Research on multisensory responses with cell-type-selective wide-field calcium imaging

細胞種選択的広域カルシウムイメージング法による多感覚刺激応答の研究

March 2018

Satoshi KUROKI

黒木　暁

Research on multisensory responses with cell-type-selective wide-field calcium imaging

細胞種選択的広域カルシウムイメージング法による多感覚刺激応答の研究

March 2018

Waseda University

Graduate School of Advanced Science and Engineering

Department of Life Science & Medical Bioscience

Research on Molecular Brain Science

Satoshi KUROKI

黒木 暁

Contents

Abstract

Multisensory integration (MSI) is a fundamental emergent property of mammalian brain. During MSI, perceptual information encoded in patterned activity is processed in multimodal association cortex. However, the systems-level neuronal dynamics that coordinate MSI remain unknown. Here, I demonstrate that association cortex contains intrinsic hub-like network activity that regulates MSI. I engineered novel calcium reporter mouse lines based on the fluorescence resonance energy transfer sensor Yellow Cameleon (YC2.60) expressed in excitatory or inhibitory neurons. In medial and parietal association cortex, I observed spontaneous slow waves that self-organized into hubs defined by long-range excitatory and local inhibitory circuits. Unlike directional source/sink-like flows in sensory areas, medial/parietal excitatory and inhibitory hubs had net zero balanced inputs. Remarkably, multisensory inputs triggered rapid phase-locking of excitatory hub activity persisting for seconds after the stimulus. Therefore, association cortex has a propensity to form balanced excitatory networks that configure slow wave phase-locking for MSI.

Chapter 1 Introduction

Multisensory integration

Multisensory integration (MSI) involving the synthesis of neural information from cross-modal sensory stimuli may complement responses from individual modalities and enhance behavioral performance (Stein and Stanford, 2008). Multisensory responses observed many regions in the brain and can be roughly divided into two types of responses, amplitude (Stein and Stanford, 2008; Ghazanfar and Schroder, 2006) and phase (van Atteveldt et al., 2014) modulation. The amplitude modulation is that the response amplitude of a recording signal to multisensory simultaneously stimulus exceeds summation of responses to two or more single modal sensory stimuli (non-primary sensory area) or modulates responses to representative input with non-representative input (primary sensory area) (Schroeder and Foxe, 2005). On the other hand, the phase modulation is that alignment of ongoing oscillations with a sensory stimulation among trials and degree of the alignment can be enhanced with multisensory stimuli (van Atteveldt et al., 2014).

The amplitude-modulation type responses were observed in superior colliculus (Meredith and Stein, 1983), striatum (Reig and Silberberg, 2014), and cerebral cortex (Ghazanfar and Schroder, 2006). In the cortex of primate and human, the multisensory responses were not reported only in parietal and frontal association cortices (Bruce et al., 1981; Duhamel et al., 1998; Sugihara et al., 2006) but also in primary sensory areas (Schroeder and Foxe, 2005). In the rodents, the amplitude modulation was not observed in the association cortical areas, but reported in border regions between primary sensory cortices (Brett-Green et al., 2003; Lippert et al., 2013; Olcese et al., 2013; Wallace et al., 2004) and insula cortex (Gogolla et al., 2014).

The phase-modulation type responses were observed only in the primary sensory area of the cerebral cortex, which is called phase reset (Kayser et al., 2008; Lakatos et al., 2007; Sieben et al., 2013). Phase relations of cortical oscillations are crucial for intercortical communications (Varela et al., 2001). The phase reset was observed mainly in the lower-frequency, delta and theta band (Schroeder and Lakatos, 2009), and can be an underlying mechanism of associating temporal

synchronized sensory inputs, for example, the cocktail party effect (We can hear a certain person's voice even in a very noisy environment such as cocktail party) implies associating fluctuations of a mouth movement and a hearing voice (van Atteveldt et al., 2014). Phase relationship between distant areas mediates gating of information between the areas (Fell and Axmacher, 2011). Whereas Gamma-band (30-80 Hz) oscillations are committed to feature binding across modalities and selective attention is based on phase synchronization, slow-wave oscillation (<1 Hz) propagates through the entire cortex and is thought to be involved in information transfer, sensory amplification, and attention (Schroeder and Lakatos, 2009).

Additionally, cell-type specific functions were also observed in some of the multisensory regions (Gogolla et al., 2014; Olcese et al., 2013). In the border region between V1 and S1 area, only pyramidal excitatory neurons have somatosensory-visual multisensory response property and parvalbumin (PV) inhibitory neurons modulate the pyramidal neuronal responses to multisensory stimulus (Olcese et al., 2013). Activity of inhibitory neurons in the insula cortex in a developmental period is critical for organizing multisensory responsiveness of the insula (Gogolla et al., 2014).

As described above, multisensory responses were reported in various brain regions and interactions among the regions can be important for the MSI, but it is unclear how they interact. A problem of previous studies is that they recorded from one or few points of the brain, though the MSI seems to be achieved by interaction among many brain regions. I thought the wide-field imaging method could solve the problem and reveal the interregional interactions for the MSI.

Wide-field imaging methods

Wide-field imaging methods are powerful tools for viewing intercortical activity. Several methods are available using intrinsic signals, chemical dye and genetically encoded sensors.

Intrinsic imaging methods use hemodynamics (Lippert et al., 2013; Olcese et al., 2013; Schuett et al., 2002) or flavoprotein fluorescence (Gogolla et al., 2014; Hishida et al., 2014; Yoshitake et al., 2013) as physiological recorded signals. These signals can record with high spatial resolution

compared to other neural recoding methods such as electrophysiological recording and also achieve transcranial imaging, recording through the intact mouse skull and being low invasiveness. It has, however, low temporal resolution compared with neuronal signals because they are kinds of metabolic signals and the fluctuations are very slow.

Using extrinsic inductions of voltage-sensitive dyes (Ferezou et al., 2007; Manita et al., 2015; Mohajerani et al., 2013) and calcium indicators (Busche et al., 2015; Stroh et al., 2013), we can achieve wide-field imaging of neural activities with high spatiotemporal resolution. The limitations of these methods, however, are the lack of cell-type selectivity and invasiveness of the dye loading.

Cell-type specific expression methods of genetically encoded voltage-sensitive and calcium-sensitive fluorescence sensors can overcome these limitations. Many types of genetically encoded sensors were developed to detect calcium fluctuations. The sensors can be introduced with viral vectors (Andermann et al., 2011; Minderer et al., 2012), electroporation (Bellay et al., 2015; Carandini et al., 2015; Tsutsui et al., 2013) and creating transgenic (Tg) animals (Allen et al., 2017; Madisen et al., 2015; Makino et al., 2017; Murakami et al., 2015; Vanni and Murphy, 2014; Monai et al., 2016). Except Tg method, it is difficult to stably control the expression level, duration, and locus of the target genes, and the use of Tg mice for wide-field imaging is still limited mainly to excitatory networks (Madisen et al., 2015; Murakami et al., 2015; Vanni and Murphy, 2014; Makino et al., 2017). Imaging of other cell populations like astrocytes (Monai et al., 2016) or inhibitory neurons (Allen et al., 2017) were reported very recently. I improved this method to observe signals from more minor cell population in the brain.

Genetic techniques for improving cell-type selectivity and signal sensitivity

We should consider several aspects of the method to extract fluorescence signals from smaller cell populations, and I will focus on genetic techniques about three points, cell-type selectivity, gene expression level and genetically encoded sensors.

Various gene techniques were developed to express target genes in specific cell populations, such as cell-type specific gene promoters, Cre/LoxP and Tet systems (Luo et al., 2008). Cell-type specific promoters can work in specific types of cells, which express the original genes, for example the Tau promoter works in pan-neuron (Binder et al., 1985), Emx1 works in the telencephalon excitatory neurons and astrocytes (Iwasato et al., 2000) and VGAT works in inhibitory neurons (Ogiwara et al., 2013). The Cre/LoxP and Tet systems are more complex. In the Cre/LoxP system, Cre protein cuts a DNA sequence flanked by the LoxP sequence (floxed) and regulates the floxed or downstream gene expression and Cre proteins are expressed under the control of a cell-type specific promoter. The Tet system is similar that target gene expressions are regulated by the Tet operator (TetO) protein expression and the TetO expresses under the control of a cell-type specific promoter. One of the advantages of the Cre/LoxP and Tet systems is that, after establishing Tg mice lines, we can create various types of Tg mice for many experimental purposes with just crossing driver (Cre and TetO expressing) and reporter (target gene expressing) Tg mice. Many groups developed driver (Harris et al., 2014) and reporter (Madisen et al., 2015) Tg mice, and we can label, monitor and manipulate in cell-specific functions by just crossing those mice.

The target gene expression level of a Tg mice line is affected by various factors such as the promoter activity, messenger RNA (mRNA) stability and inserted genome locus. In my study, I tried and achieved to increase the expression level of the calcium sensor by stabilizing mRNA. I used a Simian virus 40 (SV40) intron containing a splicing signal (Palmiter et al., 1991) and Woodchuck hepatitis virus posttranscriptional regulatory element (WPRE) (Choi et al., 2014) both of which stabilize the mRNA structure.

Many genetically encoded probes were developed to detect calcium or voltage signal. Intracellular calcium concentration of neuron rises 10 to 100 times higher in actives states than in resting state (Berridge et al., 2000), and it makes us easy to detect the neuronal activities. The most major genetically-encoded calcium indictor (GECI) is GCaMP (Grienberger and Konnerth, 2012). GCaMP is a single fluorescence protein-based sensor and has high fluctuation ratio and

fast kinetics (Chen et al., 2013). Some of Tg mice for wide-field calcium imaging (Murakami et al., 2015; Vanni and Murphy, 2014) use GCaMP3 as a calcium probe. However, it is hard to remove the noise component, which derives from respiration, pulsation and body movements, because GCaMP is a single protein based sensor, and it is difficult to distinguish between signals originating from neural activity and noise. Another major calcium indicator is Cameleon (Nagai et al., 2004; Horikawa et al, 2010). Cameleon is a fluorescence resonance energy transfer (FRET) based calcium-sensitive fluorescence protein, which can reduce the noise component with a ratiometric procedure of two fluorescence signals from accepter and donor fluorescent proteins. Noise extraction methods based on the FRET system were developed in some groups (Akemann et al., 2012; Carandini et al., 2015). Additionally, Cameleon showed relatively higher affinity to calcium than GCaMP (Chen et al., 2013; Grienberger and Konnerth, 2012; Horikawa et al., 2010). Some variants of Cameleon can detect lower concentration calcium fluctuation, possibly sub-threshold fluctuation.

To advance wide-field calcium imaging technology, I established a novel transgenic (Tg) mouse line that expresses Yellow Cameleon 2.60 (YC2.60) (Nagai et al., 2004), a variant of Cameleon, in selective neuronal populations using the Cre/loxP system. To increase cell-type selectivity, restricting only to neurons, I use the Tau BAC promoter (Binder et al., 1985). I also combined a SV40 intron (Palmiter et al., 1991) and the WPRE sequence (Choi et al., 2014), to increase YC2.60 expression and detect the fluorescence signals more effectively. With these techniques, I achieved to detect calcium signals from small neural populations, inhibitory neurons whose cell density is around 1/5 of excitatory one.

I sought to advance the technologies to analyze wide-field cell-type-specific cortical dynamics, by establishing novel Tg mouse lines that express YC 2.60 in selective neuronal populations using the Cre/loxP system. After crossbreeding the YC2.60 mouse with Emx1-Cre (Iwasato et al., 2000) and VGAT-Cre lines (Ogiwara et al., 2013), respectively, I was able to observe clear neural activity

in excitatory and inhibitory networks *in vivo*. In parallel with the Tg lines, I also developed novel analytical methods to specifically extract neural activity from broadband calcium signals, thereby achieving quantitative wide-field imaging of both excitatory and inhibitory neuronal populations. I found that intercortical spontaneous connectivity for excitatory networks was broader than that of inhibitory networks and slow waves showed a balanced flow in and out of hub-like centers in medial and parietal association cortices. Global responses to multisensory stimuli could be computed as combinations of responses to each unimodal stimulus regardless of the cell type. Nevertheless, in excitatory networks, multimodal stimuli produced phase-locking of ongoing cortical slow oscillations for several seconds after stimulation at medial/parietal association cortex regions, suggesting that MSI employs balanced excitatory network hubs.

Chapter 2　Materials and Methods

Animals

All experimental procedures were performed in accordance with the guidelines of the RIKEN Institutional Animal Care and Experimentation Committee. All studied mice were on the same C57Bl6J genetic background, 3-8 month of ages.

DNA construction

The YC2.60 sequence was extracted by polymerase chain reaction (PCR) amplification from YC2.60/pRSETB (Nagai et al., 2004) using Phusion High-Fidelity DNA Polymerase (Finnzymes) with primers containing restriction enzyme recognition sequences, and the Kozak sequence additionally in the sense primer, at the 5'-end of 20-base pair (bp) complementary sequences. The Kozak-YC2.60 sequences were inserted downstream of the LoxP-Stop(pgk-neo-polyA)-LoxP (LSL) sequence (Gene Bridges), followed by insertion of the woodchuck hepatitis virus posttranscriptional regulatory element (provided by Dr. Karl Deisseroth), the SV40 small T antigen intron (providing the splice signal), and a polyA sequence (derived from the pMSG cloning vector, Genebank Accession Number U13860) into the pHSG397 vector (Takeshita et al., 1987) using Ligation high (TOYOBO). The LSL-YC2.60 cassette was inserted downstream of the *Tau*-promoter sequence of a bacterial artificial chromosome (BAC) clone RP23-344E9 (BACPAC Resources Center) using the Red/ET recombination technique (Gene Bridges). The woodchuck hepatitis virus posttranscriptional regulatory element and SV40 small T antigen intron sequences were used to stabilize mRNA and increase YC2.60 protein expression, and the *Tau* BAC promoter was used to restrict YC2.60 expression to only neurons (Binder et al., 1985). The *Tau*-LSL-YC2.60 BAC-DNA was linearized and injected into the pronuclei of zygotes of C57BL/6 inbred mice at 2 ng/μl. Genotyping of the LSL-YC2.60 mice was performed by PCR using universal green fluorescent protein primers (forward primer, 5′-AAGGGCGAGGAGCTGTTCAC-3′; reverse primer, 5′-

GTCGTCCTTGAAGAAGATGG-3′; for 303-bp products or forward primer, 5′-AAGATCCGCCACAACATCG-3′; reverse primer, 5′-TTCTCGTTGGGGTCTTTGCT-3′; for 146-bp products).

Transgenic line selection and mouse generation

Each LSL-YC2.60 transgenic mouse line was bred with Emx1-Cre knock-in (ΔNeo) mice (Iwasato et al., 2000) expressing Cre in the excitatory neurons of the telencephalon. The double transgenic animals were deeply anesthetized with 0.5 ml of 2.5% tribromoethanol (Sigma-Aldrich) and intracardially perfused with cold 4% paraformaldehyde (Nakalai Tesque) in 0.1 M phosphate buffer, pH 8.0. Brains were dissected out from the skull and postfixed for 1 h with the same fixative on ice. Sagittal sections were cut into 100-μm thick sections with a Linear-slicer (Dosaka) and mounted onto slides with Immu-Mount (Thermo Fisher Scientific). Images of the sections were digitized using a virtual slide scanner (NanoZoomer-RS C10730-2, Hamamatsu Photonics). I selected transgenic mouse lines by comparing the spatial expression patterns and fluorescence intensities of the acquired images of each line. The selected tLSL-YC2.60 mice were crossed with Emx1-Cre knock-in (ΔNeo) and VGAT-Cre transgenic mice (Ogiwara et al., 2013) to generate Emx1-YC and VGAT-YC mice, respectively.

Immunohistochemistry

Animals were deeply anesthetized with 0.5 ml of 2.5% tribromoethanol and intracardially perfused with cold 4% paraformaldehyde in 0.1 M phosphate buffer, pH 8.0. Brains were dissected out from the skull and postfixed for 1 h with the same fixative on ice. The brains were equilibrated at 4°C overnight in 15% sucrose, again overnight in 30% sucrose, and then frozen in OCT compound (Sakura FineTeck Japan). The samples were sliced at a 30-μm thickness with a cryostat (HM560, Thermo Fisher Scientific).

For anti-CaMKIIα staining, the tissue sections were preincubated in 0.8% Block Ace (DS Pharma Biomedical) or 5% normal goat serum in phosphate-buffered saline (PBS) containing 0.1% TritonX-100 (PBST) for 1 h and incubated with mouse anti-CaMKIIα (05-532; Millipore; 1:500) antibodies/0.4% Block Ace (or 5% normal goat serum) in PBST buffer in a cold room overnight. After incubation with Alexa 594-conjugated goat anti-mouse IgG (H + L) (Life Technologies; 1:500)/0.4% Block Ace in PBST buffer at room temperature for 1 h, the slices were mounted onto MAS-coated glass slides (Matsunami Glass Ind., Ltd.) with Hard-Set Mounting Medium containing 4',6-diamidino-2-phenylindole (Vector Laboratories) or Shandon Immu-Mount (Thermo Scientific). For anti-GABA staining, I used rabbit anti-GABA primary antibodies (A2052, Sigma-Aldrich; 1:1000) and Alexa 594-conjugated goat anti-rabbit IgG (H + L) (Life Technologies). For anti-S100β staining, I used rabbit anti-S100β (37a, Swant; 1:1000) or mouse anti-S100β (SH-B1, Sigma; 1:1000) as the primary antibody, and the secondary antibodies were the same as the above Alexa-594 antibodies. For double-staining of CaMKIIα and S100β, or GABA and S100β, I used Alexa 647-conjugated goat anti-rabbit IgG (H + L) (Life Technologies) or Alexa 647-conjugated goat anti-mouse IgG (H + L) (Life Technologies) as the secondary antibody for anti-S100β. Naïve YC2.60 (Venus) and Alexa (594 or 647) fluorescence were viewed by laser confocal scanning microscopy (FV1000D, Olympus). The Venus- and Alexa-positive cells were counted manually using an ImageJ plug-in, Cell Counter (https://imagej.nih.gov/ij/plugins/cell-counter.html).

Wide-field imaging

The mice were implanted with a stainless-steel chamber plate on the head and the skull was coated with clear dental cement (Super-bond C&B, Sun Medical) for transparentization under ketamine (50 mg/kg) and xylazine (25 mg/kg) anesthesia. The head plate was tilted at about 9.5° from the horizontal line to view the left auditory cortex. After at least 1 week recovery, the head plate was fixed to head clamp apparatus and the cortical activity was observed transcranially under a mixture of fentanyl (0.05 mg/kg), midazolam (5.0 mg/kg), and medetomidine (0.5 mg/kg)

anesthesia (fentanyl-anesthetized condition, Figure 2B). In the isoflurane-anesthetized condition, the mice were weakly anesthetized with 0.8% isoflurane. In the awake condition, after experiments were performed or just a mouse was set under the microscopy in the isoflurane-anesthetized condition, the isoflurane exposure was terminated and spontaneous movement of the mice was confirmed after several minutes. Body temperature was maintained at approximately 37°C with a heating pad (ATC-402, Unique Medical). During the imaging, heart beat and respiration rate were monitored at 1-kHz sampling frequency with a photoreflector (RPR-220, Rohm) attached to the hindlimb and with a piezoelectric film (LDT0-028K, Measurement Specialties) underneath the chest, respectively, installed on an open source microcontroller (Arduino Uno). This imaging method enabled the chronic observation of the cortical activity for several months.

The cortical hemispheres were illuminated with an excitation light through a blue bandpass filter (438/24 nm, Semrock) from a 250W metal halide lamp (IMH-250, Sigma Koki) (Figure 2A). Fluorescence from the cortex was converged with a photographic lens (f = 50 mm F/1.2, Nikon), longer wavelength light was passed through a dichroic mirror (510 nm, Chroma) and an emission filter (542/27 nm, Semrock), and shorter wavelength light was reflected on the mirror and passed through another filter (483/32 nm, Semrock). The longer and shorter wavelength fluorescence derived from Venus and ECFP, respectively. The two types of light were converged again with another set of the same lenses and focused onto two charge-coupled device (CCD) cameras (Falcon 2M30, Dalsa), individually. All of these instruments were equipped with a multiaxial tandem-lens microscope that Dr. Takamasa Yoshida originally developed (Sigma Koki; Yoshida et al., 2012). Image frames from the two cameras were captured simultaneously at 800×600 pixels, 10 bits, and 30 frames per second with a frame grabber (Xcelera-CL PX4 Dual, Dalsa) using a computer.

Flavoprotein autofluorescence and optical intrinsic signal imaging

Preparation of mice and micrograph image reconstruction were the same as that for wide-field imaging, except for the addition of filter sets for excitation and emission lights. In flavoprotein autofluorescence imaging, the excitation lights were produced with a bandpass filter (470/40 nm, Chroma) and the emission lights were detected with another filter (525/50 nm, Chroma). In optical intrinsic hemodynamic signal imaging, the illumination lights were generated with a bandpass filter (605/15 nm, Semrock) and reflectance was collected through a second same bandpass filter.

Electrophysiological recording

For local field potential recording in the S1BFc, after wide-field calcium imaging to extract the target region responsive to whisker stimulation, a craniotomy (φ ~2 mm) was performed at that location with a dental drill. A fragment of the skull was removed, and the dura was carefully removed with a bent 27-gauge hypodermic needle. The mouse was set under the microscope and a glass pipette electrode (< 1 MΩ; GC150F-10, Harvard Apparatus) filled with an artificial cerebrospinal fluid (aCSF) containing following (in mM): 125 NaCl, 2.5 KCl, 1.2 NaH_2PO_4, 2 $CaCl_2$, 1 $MgCl_2$, 25.7 $NaHCO_3$, 25 D-(+)-glucose was inserted using a manipulator system (MP-225, ROE-200, MPC-200, Sutter Instrument Co.) while checking the fluorescence images of the microscopy. The pipette was inserted into the target region 200 to 300 μm from the brain surface. The mouse head plates were filled with aCSF. Data were acquired with a MultiClamp700B amplifier, Digidata1440A digitizer and Clampex 10.4 software (Molecular Devices), with 10 kHz sampling rate, filtered at 4 kHz with a Bessel filter and 200–500x gain. For local field potential and multiunit recording in the V1M area, I identified the V1M area with response pattern to visual stimulation of the wide-field calcium imaging. A silicon probe (1.2~1.7 MΩ; Buszaki32, Neuronexus) was inserted into the target region 200 to 400 μm from the brain surface while checking the fluorescence images of the microscopy. Data were acquired with a Digital Lynx 4SX and Cheetah software (Neuralynx), with 32 kHz sampling rate, filtered between 0.1 and 9 kHz band-pass. To identify multiunit activities, I filtered the recording signals with 300 – 5k Hz band-pass filter, selected a channel, which had the largest

unit activities, and detect spikes by thresholding with 4 or more standard deviations of the normalized traces. Firing rate was computed within 200 ms time window and normalized the mean and standard deviation through each trial. Local field potentials were 10 Hz low-pass filtered signals of the channel. Onsets of image acquisition and sensory stimulus were also recorded to adjust the Ca^{2+} FRET signal traces and the local field potential traces for offline analysis.

Multisensory stimulation

Mechanical deflection of a piezoelectric actuator (CMBP05, Noliac) was delivered to the whiskers (B1, C1, C4, D2, E1, and E3) contralateral to the target hemisphere. All of the other whiskers were removed. An individual whisker was inserted into the lumen of a blunt needle (27G, Nipro) that was attached to the actuator and the tip of the needle was placed 5 mm from the face (Figure 2C). The actuators were controlled to generate a 10-Hz square-wave pattern at an angle of deflection of ~0.2 to 15° with the drivers (NDR6110, Noliac) and Arduino microcontroller. I individually stimulated six whiskers to reconstruct the whisker map and three whiskers, e.g., C1, E1, and E3, were simultaneously evoked under other conditions. The deflection was measured in advance with a laser displacement meter (IL-S025 / IL-1000, Keyence). In awake condition, whiskers were stuck to the blunt needles with instant glue, and a shield was placed to protect the blunt needles because the whiskers could be removed by whisking or touching with forelimbs of the mouse.

Pure tones (5.7, 9.5, 11.3, 16, 19, and 22.6 kHz) and white noise (flat from 1 Hz to 100 kHz) were presented from a speaker (Companion2 III, Bose) located 13 cm in front of the mouse's nose (Figure 2C), and amplitude-modulated with a 20-Hz sinusoidal envelope (Takahashi et al., 2006). The pure tones and white noise were generated with a direct digital synthesizer (AD9834, Analog Devices) and a Zener diode, respectively. Amplitude modulation was created with a 12-bit digital-to-analog converter (MCP4922, Microchip) and the volume was controlled with a sound attenuator (NJW1159, New JRC) and an Arduino microcontroller. Pure tones of 70-dB sound-pressure level (SPL) were used to reproduce the tonotopic map, whereas the white noise varied from 55 to 85 dB

SPL for the other conditions. The SPL of each stimulus and ambient sound were measured in advance at the location of the mouse's head with a sound-level meter (Type 6224, Aco). The background sound level was ~50 dB.

A red light-emitting diode (LED; λ = 637 nm, φ5 mm, OptoSupply) emitted light flickering at 10 Hz (a square wave with 50-ms on and 50-ms off) on the mouse's right eye trough an aluminum tube, which placed the tip of the LED 10 mm from the eye (Figure 2C). The illumination intensity was varied from ~0.3 to 13 mW/m^2 during the light on using a current source (LT3092, Linear Technology) and an Arduino microcontroller. Irradiance was measured in advance with a spectrometer (ColoMeter, Spectra Co-op). To test the retinotopic map, I used a drifting grating stimuli. For stimulation, a liquid crystal display monitor (10.4 inch, DuraVision FDX1001, Eizo) was placed ~15 cm apart from the right eye, in which the angle between the screen and the mouse's midline was set at 45° (Figure 2A). Square-wave gratings (spatial frequency, 0.05 c/d; temporal frequency, 1 Hz) drifting back and forth every 1.5 s in six orientations (0–150° at intervals of 30°) were produced with an open-source programming language, Processing (http://processing.org). The luminance of the white bars of the grating was ~14 cd/m^2, black bars 1.0 cd/m^2, and gray background 2.8 cd/m^2 on the screen. The oriented gratings were presented in random order at one region divided into six equal parts vertically on the screen. The luminance of the screen was determined in advance with a luminance meter (ColoSuke, Spectra Co-op).

An experimental trial comprised a pre-stimulus period, a subsequent response period, and a post period every 5 s, in which the onset of the response period coincided with that of the stimulation. The duration of each stimulus was set at 5 s for the grating stimulation and 500 ms for the other conditions. Several trials of different stimulus conditions were repeated continuously in pseudo-random order every 6 or 24 times. Imaging of the spontaneous activity without any stimulus preceded trial blocks of all other conditions in a daily session. The control of the trial sequence was synchronized with the image frame-grabber using custom-made software. The master Arduino microcontroller received trigger signals from the computer for the imaging and controlled each

stimulator using custom software written in Processing. The face and forelimbs of the mice were viewed with a web camera equipped with infrared LEDs (GR-CAM130N2, Groovy).

For multisensory stimulation, to determine stimulation parameters that adequately evoke cortical responses in different sensory modalities, I measured stimulus intensity - response functions, also called neurometrics, and defined the optimal intensities so that the metrics would not be excessive for each individual modality as follows: whisker stimulation (S), ~1.6° deflection of three whiskers; auditory stimulation (A), amplitude-modulated white noise of 80 dB SPL; and visual stimulation (V), ~0.6 mW/m^2 flickering LED light. Combinations of sensory stimuli composed of S, S+A, S+V, S+A+V, A, A+V, and V were presented at the same onset in the trial sequence. Additionally, considering the latency of the evoked response in the visual cortex compared with the other modalities (Mohajerani et al., 2013; Wallace et al., 2004), I prepared a visual stimulus in which the onset preceded the other stimuli by 30 ms (Vp) and combined the other modalities as follows: S+Vp, S+A+Vp, and A+Vp.

Muscimol injection

After wide-field calcium imaging to extract the target region responsive to whisker stimulation, a craniotomy (φ ~2mm) was performed at an appropriate location with a drill. After removing a fragment of the skull, the dura was carefully removed with a bent 27G hypodermic needle. The mouse head plates were filled with aCSF. Before muscimol injection, multisensory response images were acquired as controls. Muscimol (0.1 μl of 10 mM, Wako Pure Chemical) in PBS buffer was pressure-injected through a glass capillary (φ ~30 μm; B100-75-10, Sutter Instrument). The pipette was inserted into the target region 200−300 μm from the brain surface. About 10 minutes after the injection, multisensory responses were imaged again.

AAV purification and injection

Viruses were produced using a triple-transfection, helper-free method (Samulski et al., 1989) and purified using ultracentrifugation (Zhang et al., 2010). The 293 FT cells (Invitrogen) were cultured in 30 ml D-10 Complete Medium (Dulbecco's modified Eagle's medium containing 10% heat-inactivated fetal bovine serum, 1 mM sodium pyruvate solution, 0.075% sodium bicarbonate solution, 1% penicillin-streptomycin-L-glutamine solution) in 225 cm^2 cell culture flasks (Nunc, 159934) at 37ºC/5% CO_2, until the 293 FT cells reached approximately 70 to 80% confluence. They were transfected with pHelper, pAAV-DJ8 (Cell Biolabs), and pAAV-CaMKII–mCre (Codon-optimized Cre for mammalian, Koresawa et al., 2000; provided by Dr. Joshua Johansen of RIKEN BSI). Plasmids (20 μg) were mixed with 293fectin transfection regent (Invitrogen) in 300 μl Opti-MEM (Invitrogen) and incubated for 30 min at 25ºC before the mixture was transferred to 70–80% confluent 293 FT cells. After 3 days incubation at 37ºC/5% CO_2, the lysate was collected and pelleted by centrifugation for 30 min at 2500 rpm, followed by filtration with 0.45-μm filters (Millix). The cleared lysate was moved into ultracentrifuge tubes and 20% sucrose/PBS solution was added to the bottom of the tubes before centrifuging in a SW-28 rotor (Beckman Coulter) at 22,000 rpm at 4ºC for 2 h. After pouring out the supernatant, viruses at the bottom were eluted with 100 μl of cold PBS. The final purified viruses were stored at -80ºC. Genomic AAV titers were determined according to the published protocol (Rohr et al., 2002) with modifications. Real-time quantitative PCR was perfumed using the THUNDERBIRD SYBR rqPCR mix (TOYOBO) and the following primers: polyA forward: 5'-GTATGGAGCAAGGGGCAAG-3', polyA reverse: 5'-AGGCGGAGATTGCAGTGAG-3'. The expected length was 109 bp.

The tLSL-YC mice were anesthetized with isoflurane and positioned in a stereotaxic frame (Angle two, Leica). AAV.DJ/8-CaMKII-mCre (3.32×10^{11} genome copy/ml) were injected in the left hemisphere around the following coordinates; M2r: from Bregma, ML, -0.92 mm, AP, 1.14 mm; M2c: ML, -0.9 mm, AP, -1.03 mm; S1BFc: ML, -3.11 mm, AP, -1.55 mm. I injected the viruses into M2r and M2c for PLF analysis of multisensory stimulus, and into S1BFc for evoked response analysis to whisker stimulation. After craniotomies (~1mm) using a drill, a glass capillary (φ ~30

μm; B100-75-10, Sutter Instrument) was placed around each site (300 μm depth from the pia), where it could avoid blood vessels, and 0.2 μl-purified virus was delivered to each site (0.1 μl/min). After the injection, the capillary was held in place for an additional minute to allow the virus to diffuse in each region. The holes were covered with 1% agarose (Agarose-HGS, Nakalai Tesque) and a cover slip (custom made φ3 mm, Matsunami). All animals were allowed 3 weeks to recover and express YC2.60 gene before calcium imaging.

Data preprocessing

All data were processed and analyzed with MATLAB. Imaging data were resized to 400×300 pixels with 2×2 binning. Image frames were aligned to a reference image that was the first frame using TurboReg (http://bigwww.epfl.ch/thevenaz/turboreg), a Java plug-in for NIH ImageJ. Venus image was also aligned to the ECFP image using a phase-only correlation method (Takita et al., 2003). The midline and bregma were determined manually from the surface structure of the skull.

Equalized ratioing with principal component analysis

To correct the difference in the fluorescence intensity of Venus and ECFP, I equalized the power of the signal component derived from the heart beat in the two signals using the following steps: (1) pixel averaging to reduce the computational cost, (2) wavelet filtering > 3 Hz to extract the faster components mainly contaminated with heart beats, and (3) principal component analysis (PCA) to identify the heart-beat signal as the primary principal component (PC1) in the Venus-ECFP signal intensity function. The slope of PC1 was approximated as 1 to become the same level of the heart-beat power in the two signals by multiplying the reciprocal of the slope to the function as a scaling coefficient. The Venus signals were divided by the ECFP signals equalized by the scaling factor. The process of singular value decomposition is shown as follows:

$$\boldsymbol{X} = \boldsymbol{U}\boldsymbol{\Lambda}\boldsymbol{V}^{T},$$

$$\boldsymbol{V} = \begin{pmatrix} v_{11} & v_{12} \\ v_{21} & v_{22} \end{pmatrix}, \qquad a_1 = v_{21}/v_{11}, \qquad s = 1/a_1,$$

where $\boldsymbol{X}$ is the time course, $\boldsymbol{U}$ and $\boldsymbol{V}$ are the left and right singular matrices, $\boldsymbol{\Lambda}$ is the singular value matrix, $\boldsymbol{v}$ is an element of the right singular matrix, a_1 is the slope of PC1, and s is a scaling factor. In the case that the slope of PC1 was greater than 1 or less than 1 due to divergence, the slope was converged on 1 by repeating process of multiplying the reciprocal of the slope, as shown below:

$$\boldsymbol{X}_{i+1} = s_i \boldsymbol{X}_i,$$

$$s = \prod_i s_i,$$

where i is the index of iterations of singular value decomposition, and finally, scaling factors in the iterations were multiplied. Additionally, components > 3 Hz in the ratio signals were reduced by wavelet denoising (Jansen, 2001).

Grand averaging

After determining the midline angle and coordinates of bregma, I turned the image axis around bregma to adjust the midline vertically and align the coordinates of the maximum responses to each stimulus to three regions of interests (ROIs) for each primary sensory area on the brain atlas (Figure 3C). Image sequences of 24 trials (6 trials for retinotopic stimulation) were averaged over trials and sessions. The frame-averaged period of 1 s before stimulus onset was subtracted from all frames as the baseline frame. Some of the subjects were used for duplicated sessions. Finally, areas of fields of view, except cortical areas, were masked in each image frame.

Detrending and ΔR/R

Pre- and post-stimulus periods were defined as the 5-s period before a stimulus onset and the 7 to 10 s after stimulus onset. For time-courses at each ROI, the baselines were determined by averaging the time traces at pre- and post-stimulus periods for each trial. Second-order fitting

curves at both the pre- and post-stimulus periods were computed by a least-squares method as trend curves and subtracted from the original time traces for each trial. The baselines of acceptor were added to the processed traces so that the baseline levels were reset to a ratio of 1. For conversion into ΔR/R, the baselines were subtracted from the detrended traces and then the residuals were divided by the baseline.

Cortical topographic map reconstruction

Pixel and temporal standard deviations (SD) in image frames during the 5 s before a stimulus onset were computed as the SD at the pre-stimulus period. Response periods for whisker and visual stimulation were defined as during the 2 s after stimulus onset, whereas for auditory stimulation, the response period was defined as from 1 to 2 s after stimulus onset. To reconstruct each topographic map, I individually selected optimal thresholds (whisker, 3 SD; auditory, 1.2 SD; visual, 1.7 SD). Image frames were averaged over the pre-stimulus period and each response period, which were defined as the base image and response image. In the response image, pixels that exceeded the level of the base image + SD threshold were identified as areas that represented map structures. The identified area maps for different stimulus conditions were superimposed on a single image.

Signal-to-noise ratio

To quantify the response intensity in time traces at a ROI, I defined the signal-to-noise ratio (SNR) as the ratio of SDs during the pre-stimulus period and the peak amplitude of the response period as follows:

$$\mathrm{SNR} = \mu/\sigma$$

where σ is the SD during the pre-stimulus period (i.e., 2-s period before stimulus onset) and μ is the peak response amplitude in the early response period (i.e., 2-s period after stimulus onset) or late response period (i.e., 2-s period after the end of the early period). When evoked responses

are greater than 1 SD at pre-stimulus baseline, the SNR will be greater than 1. The SNR was grand-averaged over trials and sessions.

Superiority index of low-frequency component

To examine frequency structures of spontaneous activity, I defined the superiority index of low-frequency component (SI_{low}) as follows:

$$\mathrm{SI}_{\mathrm{low}} = \frac{\sum P(f)_{\mathrm{low}} - \sum P(f)_{\mathrm{high}}}{\sum P(f)_{\mathrm{low}} + \sum P(f)_{\mathrm{high}}},$$

where f is frequency, $\sum P(f)_{\mathrm{low}}$ is the sum of low-frequency power from 0.2 to 0.7 Hz, and $\sum P(f)_{\mathrm{high}}$ is the sum of high-frequency power from 1 to 2 Hz. When low-frequency power is larger than high-frequency power, the index will be more than 0 and not exceed 1. The index was averaged over sessions for each ROI.

Seed-pixel correlation map

To dissect spatial relationships between spontaneous activities at each ROI and other pixels, I computed seed-pixel correlations and mapped the correlations using the following steps: (1) pixel-averaged time traces were created for each ROI (3×3 pixel region) as seed time traces, where the length of the time course was 9 min/session, (2) pixel-pairwise correlation coefficients (Pearson correlation with zero lag) were calculated between the seed time trace and time traces at all pixels region by region, and (3) the correlation coefficients were positioned onto the counterpart pixels of each seed to create a map of correlation coefficients. To test the similarity between the map patterns of the Emx1 and VGAT data, I created binary patterns of areas with a correlation coefficient > 0.5 in the maps and calculated session-pairwise correlations of the binary patterns of the same seeds within each genotype and across genotypes.

Cross-correlation in ROI-pairwise

First, pixel-averaged time traces at each ROI, 3×3 pixels, were created for each session, and then the time traces of several sessions were concatenated in the session order. I then calculated cross-correlation coefficients between all pairwise combinations of target ROIs (nodes) and the others (counterparts) from -1.5 to 1.5 s at 33-ms intervals. Finally, cross-correlation diagrams were depicted for each node, in which only pairs of cross-correlation coefficients ≥ 0.5 were linked and the cross-correlation coefficients were encoded into the width of the lines. Additionally, time lags from -100 to 100 ms were turned into pseudo colors .

Cross-correlation divergence

Considering the time lags and cross-correlations simultaneously at each node, I defined "divergence" as the index of sinks and sources of flow as follows:

$$D_i = \frac{1}{L}\sum_j (\tau_{i,j} \cdot c_{i,j}) \times 100, \qquad \text{if } c < 0.5, \text{then } c = 0,$$

where D_i is the divergence at node i; L is the constant number of all links, which is 20; j is the counterpart ROI of node i; $\tau_{i,j}$ is the time lag; and $c_{i,j}$ is a peak correlation between node i and counterpart j at the time lag. On average, values higher and lower than 0 indicate that the node is a sink or source, respectively, of activity flow. When the number of links was large but divergence was close to 0, the flows were thought to cancel out at the node. When the number of links was small and divergence is close to 0, the correlation itself did not exist at the node.

Hub-like index

To quantify hub-like properties (net-zero source/sink divergence and many high-correlation nodes) of each ROI, I defined the hub-like index by divergence and the number of links as follows:

$$H_i = \frac{max(|D|) - |D_i|}{max(|D|)} \cdot \frac{L_i}{L},$$

where H_i is hub-like index at a node i; $|D_i|$ is the absolute value of divergence at a node i; $max(|D|)$ is maximum value of absolute divergence in all ROIs; L_i is the number of high-correlation links (correlation coefficient > 0.5) at a node i; L is the constant number of all links, which is 20. The maximum value of the hub-like index is 1 when $|D_i| = 0$ and $L_i = 20$, and the minimum is 0.

Cortical parcellation with hierarchical clustering

To dissect hidden structures of spontaneous activity in the cortical space, I performed hierarchical clustering (Jain and Dubes, 1988) of time courses over the spatial extent in each session of spontaneous conditions. Cortical fields were partitioned into 3x3-pixel tiles and time courses within the individual tiles were pixel-averaged in advance of the clustering. The clustering process consisted of following three steps: (1) the clustering was conducted so that the number of clusters was decreased at 128, (2) the clustering was consequently carried out so that the number of clusters was compressed to 24, (3) the cluster arrangements were reordered based on distances between the clusters each other, where Ward's method based on the Euclidean distance was adopted as the distance function between clusters for the clustering.

Comparison of evoked responses and clustered areas

Similarity between parcellated areas of spontaneous activity by the clustering and each evoked area by whisker, visual and auditory stimuli were examined in multiple sessions. Evoked areas were specified by the followings: (1) image sequences in multiple sessions were grand-averaged in the same stimulus conditions, (2) frame-averaged images over 5-s duration before a stimulus onset were defined as base images in the pre-stimulus period, (3) frame-averaged images over 1-s duration after the stimulus onset were identified as evoked images in the response period, (4) the base image was subtracted from the evoked image, and (5) pixel areas exceed 3SD of the pixel distribution in the evoked image were chosen as evoked areas.

To select a clustered area that was the most similar to each evoked area in each spontaneous session, I defined overlap index as follows:

$$\text{Overlap index} = N_{\text{common}}/N_{\text{union}}$$

where N_{common} and N_{union} are the numbers of pixels of the intersection and union between each evoked area and all clustered areas, respectively, and a clustered area that had the largest overlap index was selected. The index is 1 when a clustered area pattern is perfectly congruent with the corresponding evoked area pattern. On the other hand, the index is close to 0 when both patterns are overlapped little each other or the area of either pattern was greatly large.

Multisensory evoked response

Each ΔR/R time trace was normalized by subtracting the mean and dividing by the standard deviation of baseline ΔR/R values (from 0 to 2 s before stimulus onset) (z-score). Early responses were defined as mean values from 0 to 2 s after stimulus onset, and late responses were defined as mean responses from 2 to 4 s. For Emx1-YC vs VGAT-YC mice comparison in Figure 8C, only datasets showing significant changes in either Emx1-YC or VGAT-YC mice (colored circles in Figures 8A and 8B) were used. For single vs multiple stimulus comparison in Figure 8D, the areas were thresholded with hub-like index > 0.5 (Figure 6E) and only significant responses were pooled for statistical analysis.

Phase-locking factor

I defined phase-locking as a phenomenon in which the phase of slow oscillation aligns between trials for several seconds after the stimulus offset so that I could discriminate this from phase resetting, which occurs within several hundred milliseconds after stimulus onset. The ΔR/R time trace of each ROI was subtracted from the mean of all the time traces for zero-crossing. To decrease delayed-decay components of evoked responses, I removed the low-frequency components in the time traces at each ROI trial by trial using a high-pass filter with a 0.5-Hz cutoff

frequency. Instantaneous phases of the traces were extracted with the Hilbert transform. I determined the phase-locking factor (PLF) (Kawasaki et al., 2014) to validate the phase alignment quantitatively. The definition of PLF follows:

$$PLF(t) = \frac{1}{N}\sum_{n=1}^{N} exp(i\varphi(t,n))$$

where N is the number of the trials in a session, i is imaginary unit, and $\varphi(t,n)$ is the instantaneous phase of each time point and trial. The PLF traces were normalized by subtracting the mean and dividing by the standard deviation of baseline PLF values (from 1 to 3 s before stimulus onset). Significant PLF values were determined by one-way ANOVA ($p < 0.05$) among means of baseline, early (from 0 to 2 s after stimulus onset), and late (from 2 to 4 s after stimulus onset) time windows and multiple comparisons (Turkey-Kramer method) with baseline values.

Similar to Figures 8C and 8D, for the Emx1-YC vs VGAT-YC mice comparison in Figure 10D, only datasets containing significant changes in either Emx1-YC or VGAT-YC mice (colored circles in Figures 10B and 10C) were used. For single vs multiple stimulus comparison in Figure 10E, the areas were thresholded with a > 0.5 hub-like index (Figure 6E) criteria and only significant responses were pooled for statistical analysis.

Chapter 3 Establishment of cell-type selective wide-field calcium imaging (Kuroki et al., 2018)

Establishment of cell-type-specific Yellow Cameleon Tg mouse lines

MSI, a phenomena that by definition involves brain-wide intracortical dynamics, is ideally studied using wide-field imaging with cell-type specificity and reliability. Several systems have been developed for wide-field calcium imaging of cortical activity using GECIs of the GCaMP family. However, a limitation of most GECIs including GCaMPs for in vivo imaging is the lack of their ability to measure relatively pure neuron-derived signals with removal of physiological noise such as circulation and respiration artifacts. The removal of non-neuronal activity signals is particularly critical for the cell-type-specific network imaging that I performed given the relatively small number of inhibitory neurons (Markram et al., 2004). To enable high resolution imaging of excitatory and inhibitory neuronal networks without contaminating signals I designed a system for neuronal cell-type-selective expression of a FRET-based GECI by generating Tg mice expressing the Yellow Cameleon reporter YC2.60 (Nagai et al., 2004) under the control of the neuronal Tau promoter to limit gene expression predominantly in neurons (Binder et al., 1985), and the Cre/loxP system, named Tau-loxP-Stop-loxP (tLSL)-YC2.60 Tg mice (Figure 1A). The YC2.60 mouse enables a large dynamic range and relatively high affinity for calcium (Kd = 95 nM, Horikawa et al., 2010), compared to GCaMPs (Kd = 144–840 nM, Chen et al., 2013; Grienberger and Konnerth, 2012). I selected the tLSL-YC2.60 line containing high levels of YC2.60 expression in cortical neurons and engineered two mouse lines, Emx1-Cre:tLSL-YC2.60 (Emx1-YC) and VGAT-Cre:tLSL-YC2.60 (VGAT-YC), for wide-field cortical imaging of excitatory and inhibitory neuronal calcium dynamics, respectively, as a proxy for neuronal activity. In the cerebral cortex, Emx1-YC mice exhibited a high level of YC2.60 expression (Figure 1B, right), and VGAT-YC mice did relatively lower levels (Figure 1C, right).

To assess cell-type selectivity, I performed immunohistochemistry of Emx1-YC and VGAT-YC mice with anti-CaMKIIα and anti-GABA immunostaining as excitatory and inhibitory neuronal markers, respectively (Figures 1D and 1E). In Emx1-YC brain slices, YC2.60-expressing cells overlapped with 98.7% of CaMKIIα-positive cells (551 of 558 cells, N = 22, n = 5), where N and n indicate the number of images and the number of subjects, respectively, and collocated with 0.8% of GABA-positive cells (1 of 119, N = 36, n = 3). In VGAT-YC mice, YC2.60-expressing cells overlapped with 96.8% of GABA-positive cells (122 of 126, N = 33, n = 4) and did not overlap with CaMKIIα-positive cells (0 of 111, N = 31, n = 3). These results confirmed the strong cell-type-selective expression of YC2.60 in excitatory and inhibitory neurons in Emx1-YC and VGAT-YC mice, respectively. I also examined neuronal selectivity of the YC2.60 expression in Emx1-YC and VGAT-YC mice by staining astrocytes. There was no overlap in either genotype between YC2.60 and cells positive for the astrocyte marker S100β (Emx1: N = 19, n = 2; VGAT: N = 12, n = 2) (Figure 1F and 1G), indicating neuronal and not glial selectivity of these Tg mouse lines.

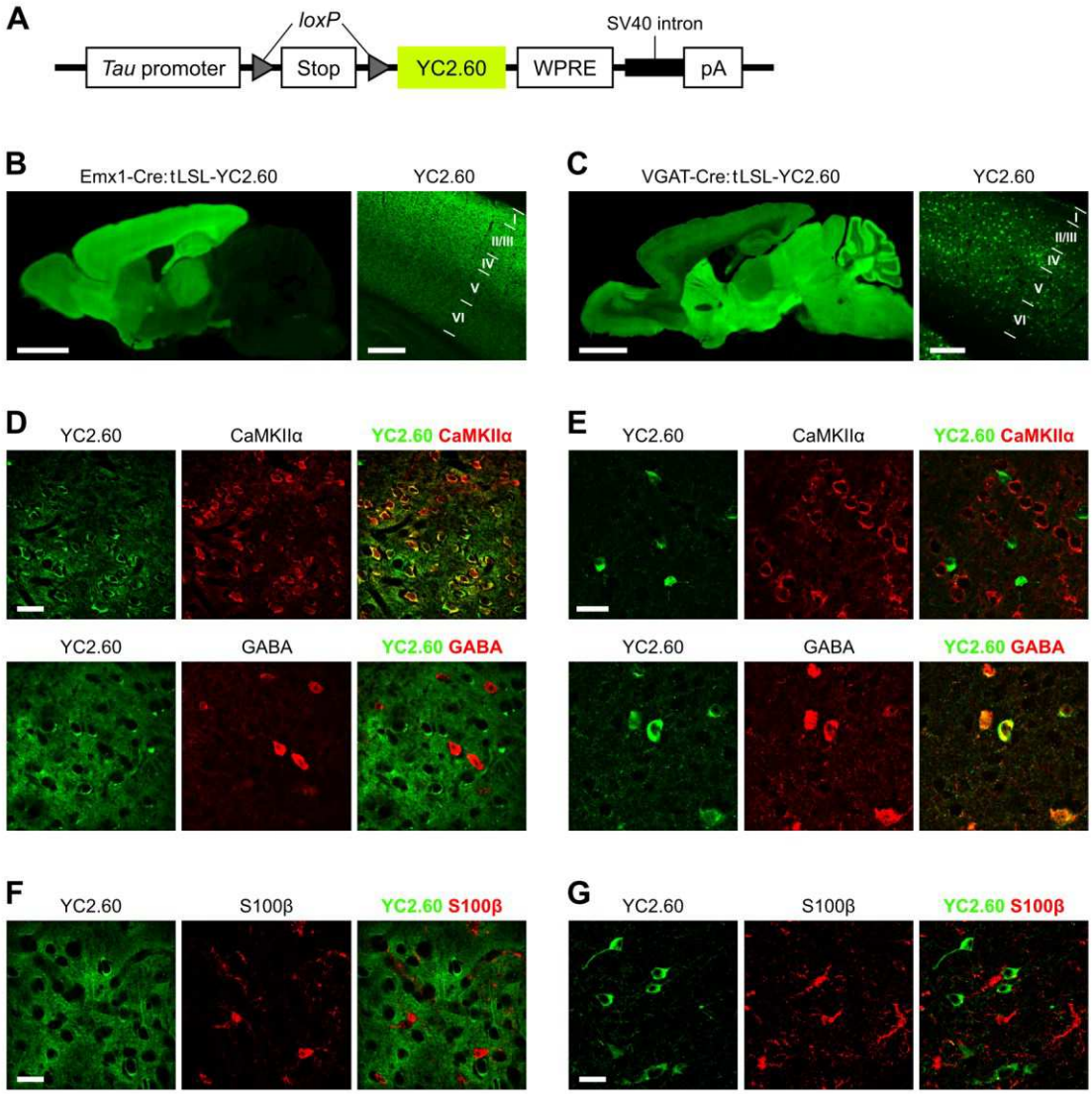

Figure 1
Establishment of cell-type-specific YC2.60 Tg mouse lines.
(A) Schematic of the YC2.60 transgene construct. The YC2.60 gene was inserted downstream of the *Tau*-loxP-Stop-loxP (tLSL) sequence.
(B and C) Low-magnification naive YC2.60 (Venus) fluorescence images of Emx1-YC (B) and VGAT-YC (C) mice. Left panels show epifluorescence images of sagittal sections and right panels show confocal images of the S1 cortical area in coronal sections. Scale bars = 2 mm (left panel) and 200 μm (right panel).
(D and E) Immunohistochemistry with anti-CaMKIIα and anti-GABA antibodies of Emx1-YC (D) and VGAT-YC (E) mice. Green and red channels indicate naive fluorescence of YC2.60 (Venus) protein and Alexa 594 fluorescence, which represents CaMKIIα (upper panels) or GABA (lower panels) protein expression, respectively. Scale bars = 20 μm.
(F and G) Immunohistochemistry of astrocytes stained with S100β in Emx1-YC (F) and VGAT-YC (G) mice. Green and red channels indicate naïve fluorescence of YC2.60 (Venus) protein and Alexa 647 fluorescence (S100β) that highlights either excitatory (F) or inhibitory (G) neurons and astrocytes. Scale bars = 20 μm.

Experimental setup for wide-field calcium imaging and procedure of image data

I applied Emx1-YC and VGAT-YC mice to wide-field calcium imaging (see Chapter 2). I used a custom-made epifluorescence tandem-lens macroscope (Figure 2A). The mice were anesthetized,

and the heads were tilted to exposure auditory areas (Figure 2B). The sensory stimulus was supplied with a speaker (auditory), piezo benders (whisker, somatosensory) and red LED light or a LCD monitor (visual) (Figures 2A and 2C). *In vivo* cortical imaging signals include neural activity and other non-neuronal physiologic components, for example, movement of the cortical surface from heartbeat and respiration rhythms. With FRET sensors like Yellow Cameleon it is in principle possible to remove such contaminating components in a ratiometric manner (Lütcke et al., 2010). This would not work, however, if the fluorescence intensities of donor and acceptor illuminants were different. The original Venus, acceptor protein, and ECFP, the donor protein, show peak signals at ~1 Hz related to the spontaneous cortical slow oscillation, and at ~4 Hz derived from the heartbeat (Figure 2D). The ratiometric (Venus / ECFP signal) results still contains the heartbeat component to some extent. Several methods have been used to extract neuronal signal components from fluorescence indicators (Akemann et al., 2012; Carandini et al., 2015). To remove noise in the FRET signals with greater stability than existing methods, I applied principal component analysis to equalize powers of noise component (around 4Hz) of donor and acceptor (see Chapter 2). The remaining heartbeat component in the original ratio signal was completely removed by ratioing after equalization of the original signals using the computed scaler (Figure 2E) and remaining noise was filtered by wavelet denoising (Figure 2F). High-pass signals from both types of fluorescence nearly coincided with pulsation signals recorded from the sole of the hindlimb (Figure 2G). Although respiration changes estimated from the displacement of the abdomen peaked at ~2 Hz, these signals did not contaminate fluorescence signals from the brain. These results suggest that my system measured pure neuronal activity signals after the removal of contaminating signals from the heartbeat and other tissues.

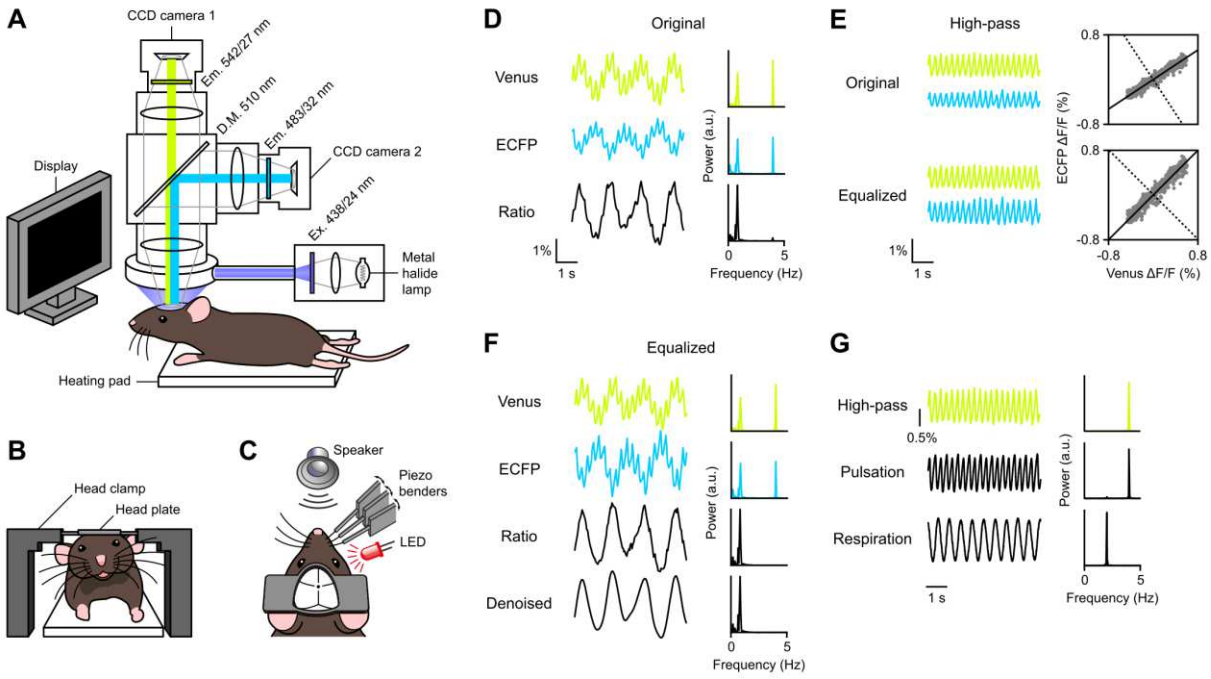

Figure 2
Experimental setup of wide-field imaging and data preprocess
(A) Schematic of the imaging setup. CCD camera 1 and 2 capture Venus and ECFP signals, respectively. Display in right front of a mouse was used for grating stimulation. DM, dichroic mirror; Em, emission filter; Ex, excitation filter.
(B) Head plate and head clamp.
(C) Multisensory stimulators. The skull inside of the head chamber was exposed and transparentized by coating with clear dental acrylic. The dot and lines on the skull represent bregma and sutures.
(D) Original time traces and power spectrum of fluorescence intensities from Venus and ECFP, and their signal ratio. The traces were pixel-averaged.
(E) High-pass traces of Venus and ECFP signals and their principal component analysis plots.
(F) Equalized traces of Venus and ECFP, and their signal ratio.
(G) High-pass trace of Venus signal and pulsation and respiration signals.
Vertical bars indicate fluorescence change (Δ*F*/*F*) for Venus and ECFP signals, and fractional change (Δ*R*/*R*) for the signal ratios.

Measurement of sensory evoked responses in primary sensory cortical areas

I first validated the robustness and reliability of calcium signals in my novel wide-field brain imaging system and using the cell-type-specific YC2.60 mouse lines. Cortical responses to whisker, auditory, and visual stimuli were measured. Image montages of trial-averaged responses in example sessions are shown in Figures 3A and 3B. Frame-averaged images over a period of one second before stimulus onset were subtracted from all frames as a base frame. Evoked responses to each sensory stimulus emerged at each expected primary cortical area in Emx1-YC and VGAT-YC mice. Twenty-one representative ROIs were determined on the brain atlas (Figure 3C). Responses to auditory stimuli were also evoked in a parietal region around S1HL and PtA, in good

agreement with previous findings (Mohajerani et al., 2013). Topographic response maps in each sensory cortex were reconstructed by grand averaging for each type of sensory stimulation (whisker: N = 8, n = 8; auditory, N = 8, n = 7; visual, N = 11, n = 7) (Figure 3D), where N and n indicates the number of sessions and the number of subjects, respectively. These topographic maps were highly consistent with the anatomical and functional areas previously identified in V1 (Schuett et al., 2002), S1BF (Akemann et al., 2010), and A1 (Kalatsky et al., 2005), indicating the high resolution of my imaging system to detect reliable cortical tuning patterns within one area.

Pixel-averaged response traces at each ROI, 3×3 pixel regions, in each primary sensory area were delineated by grand averaging (Emx1-YC, N = 9, n = 7; VGAT-YC, N = 6, n = 4) (Figure 3E). Prominent evoked responses to each type of sensory input were observed after stimulus onset in both genotypes. Evoked responses in S1 and V1 appeared as first and second peaks. The first peak was greater than the second peak in S1, and *vice versa* in V1. The first peak was likely an early response to a corticipetal input from the thalamus because of its immediate emergence after stimulus offset, whereas the second peak was likely a reverberation component. Tails ~2 s after the second peak might depend on the decay kinetics of YC2.60 (Bellay et al., 2015). In A1, a second peak appeared to be superimposed upon the first peak that was seen as an inflection point because the onset of the second peak may be earlier, within 500 ms after stimulus offset, than that in other areas. To quantify the evoked responses, I calculated the SNR (Figure 3F). Sensory responses in each area showed adequately high SNRs in both genotypes. Only visual responses significantly differed between genotypes in the late period ($p = 7.44\times10^{-8}$, Student's t-test). Response changes accompanied by stimulus-intensity changes were examined for each sensory modality by grand averaging (whisker, N = 10, n = 8; auditory, N = 9, n = 7; visual, N = 7, n = 6) (Figures 3G and 3H). Whisker and visual responses decreased exponentially as the stimulus intensities decreased linearly, whereas auditory responses decreased almost linearly as the stimulus intensity decreased exponentially. The FRET calcium signals were highly correlated to electrophysiological signals in a few cortical areas (Figure 4). Peak cross-correlation coefficient

between local field potentials and calcium signals was 0.503 ± 0.020 (lag = 200 ± 4.7 ms, mean±SEM, from 24 trials, 450 points/trial) in the S1 area, and 0.402 ± 0.027 (lag = 368 ± 12 ms, mean±SEM, from 22 trials, 450 points/trial) in the V1 area. Contamination of flavoprotein and hemodynamic signals were very low (Table 1). Taken together, these results suggest that calcium signals originating from the cortex of my YC2.60 mouse lines reflect relatively pure neuronal activity.

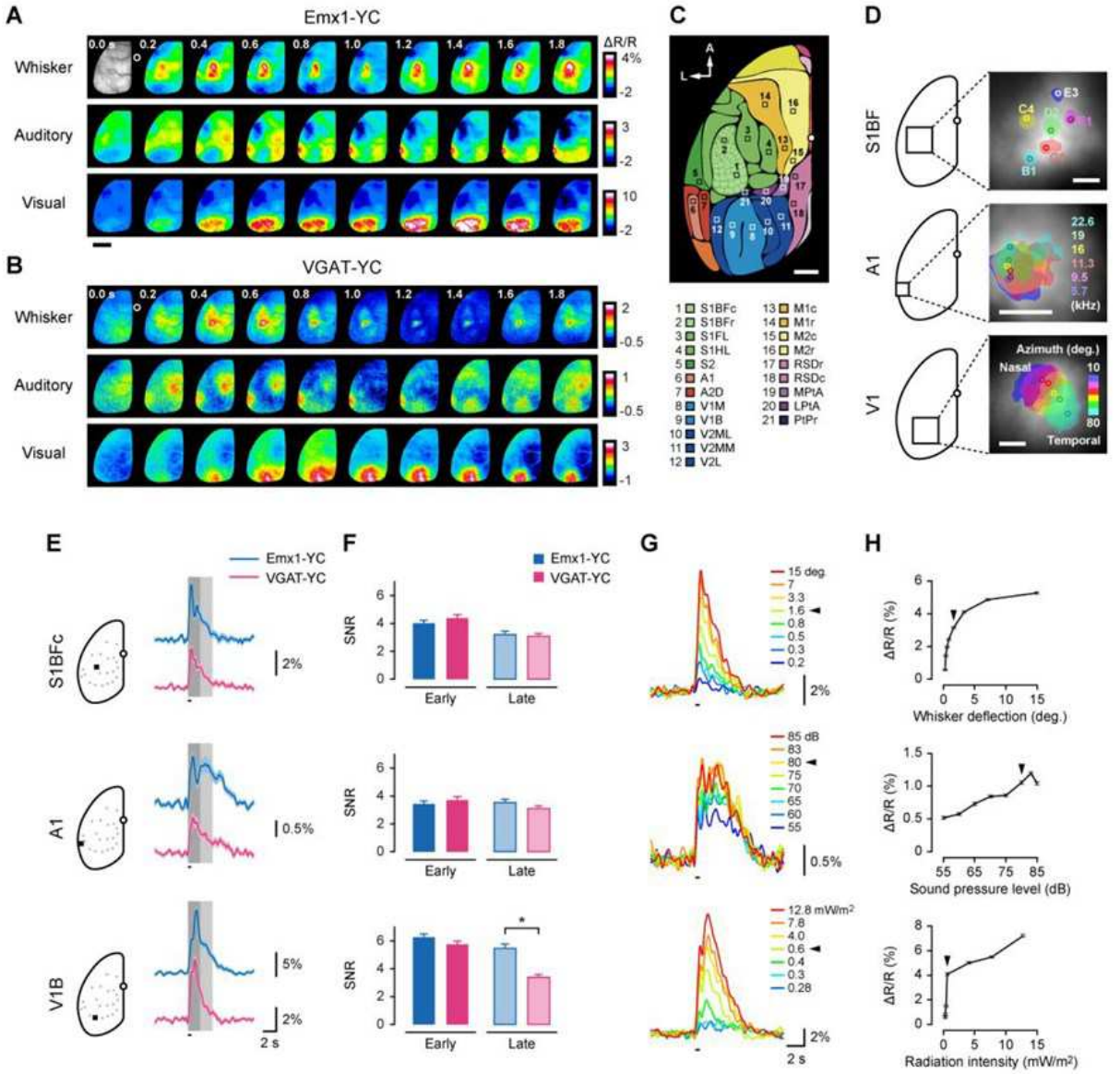

Figure 3
Evoked responses in the primary sensory areas.
(A and B) Image montage of evoked responses to whisker, auditory, and visual stimuli in Emx1-YC and VGAT-YC mice. The first frame of the whisker stimulation shows a cortical blood vessel image through the skull. Open circle indicates bregma. Scale bar = 2 mm.
(C) Overhead view of the mouse brain atlas of the left hemisphere, modified from Kirkcaldie, (2012). Open squares show locations of region of interests (ROIs). Scale bar = 1 mm. A, anterior direction; L, lateral direction. S1, primary somatosensory; -BF, barrel field; -FL, forelimb region; -HL, hindlimb region; -c, caudal part; -r, rostral part; S2, secondary somatosensory; A1, primary auditory; A2D, secondary auditory dorsal area; V1, primary visual; -M, monocular area; -B, binocular area; V2, secondary visual; -ML, mediolateral area; -MM, mediomedial area; -L, lateral area; M1, primary motor; M2, secondary motor; RSD, retrosplenial dysgranular; MPtA, medial parietal association; LPtA, lateral parietal association; PtP, parietal posterior area.
(D) Cortical sensory topographic maps in the primary sensory areas. Circles indicate maximum points of each response. Scale bar = 500 μm.
(E) Grand-averaged time courses of sensory responses to whisker, auditory and visual stimuli at ROIs of each primary sensory area. Dark and light gray hatches show 2-s early and late response periods, respectively. Black lines under the traces represent the stimulation period. Light-colored hatches indicate S.E.M.
(F) Signal-to-noise ratio of each sensory response. Error bars indicate S.E.M.
(G) Stimulus-intensity dependency of each sensory response. Arrowheads indicate parameters used in multi-sensory stimulation conditions.
(H) Neurometric function of each sensory modality. Error bars indicate S.E.M.

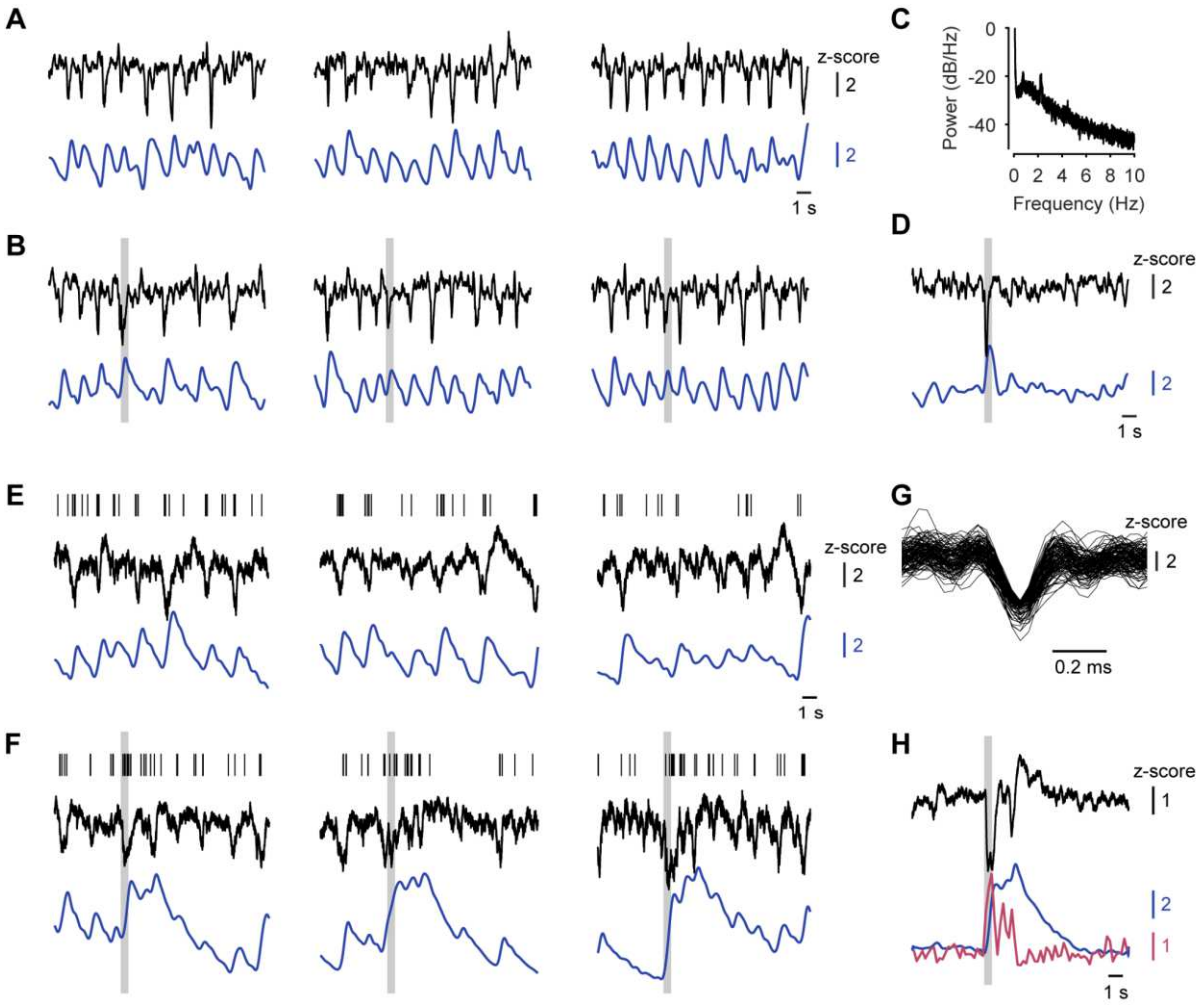

Figure 4
Local field potential and calcium signal
(A–D) Local field potentials and calcium signals in the S1BFc area.
(A) Time traces of spontaneous activities of single trials. Black and blue traces indicate local field potentials and calcium signals, respectively.
(B) Time traces of single trials during whisker stimulation. Gray bars indicate the whisker stimulation period.
(C) Power spectrum of spontaneous local field potential.
(D) Average of 24 trials during whisker stimulation.
(E–H) Multiunit activity, local field potentials, and calcium signals in the V1M area.
(E) Time traces of spontaneous activities of single trials. Vertical lines indicate the spike timings of multiunit activity.
(F) Time traces of single trials during visual stimulation.
(G) Superimposed spikes in spontaneous activity trials. Corresponding to vertical lines in (E).
(H) Average of 24 trials during visual stimulation. Red trace indicates mean normalized firing rate of multiunit activities.

		∆*F*/*F* (%)	SEM	Peak (sec)	SEM	*μ*/*σ*	SEM
Emx1-YC (n = 9)	**Y-ch**	0.505	0.0368	0.52	0.0397	6.720	0.5631
	Y-ch (negative)	-0.378	0.0494	3.41	0.2439	-4.811	0.4431
	C-ch	-0.598	0.0765	1.23	0.2512	-10.553	1.1427
	Eq-ratio	1.139	0.0713	0.56	0.0463	12.399	1.0553
	Eq-ratio (2.5s)	0.235	0.0895	2.50	0.0000	2.401	0.7267
B6 (n = 4)	**Intrinsic**	-0.053	0.00496	1.13	0.1155	-4.297	0.6501
	Flavin	0.145	0.0549	0.61	0.0886	5.046	0.8240
	Y-ch	0.049	0.0081	0.63	0.0527	2.889	0.4395
	Y-ch (negative)	-0.099	0.0140	3.33	0.4923	-5.726	0.4455
	C-ch	-0.102	0.0167	2.93	0.3689	-6.130	0.6226
	Eq-ratio	0.044	0.0145	0.77	0.0593	4.760	1.3247
	Eq-ratio (2.5s)	0.009	0.0021	2.50	0.0000	0.940	0.1507

Table 1
Comparison of flavoprotein or intrinsic signal with FRET-based calcium signals
Peak responses to whisker stimulation in the S1 area of Emx1-YC and B6 mice in FRET-based calcium, flavin (flavoprotein autofluorescence), and intrinsic signal (hemodynamics) imaging. 'SEM' stands for standard error of the mean. 'Y-ch' and 'C-ch' are yellow and cyan channels of FRET signal imaging filter sets, respectively. 'Eq-ratio' is values after equalizing and ratioing. 'Intrinsic' and 'Flavin' indicate signal values of optimal filter sets for each imaging method. μ/σ is signal-to-noise ratio, divided peak $\Delta F/F$ by standard deviance of baseline $\Delta F/F$ fluctuation in each mouse. '(negative)' indicates negative peak values. '(2.5 s)' indicates signal values at the 2.5 s after stimulus, when intrinsic signal showed large negative amplitude.

In flavin signal imaging, the peak was positive at 0.61±0.089 s (mean±SEM) after stimulation, and in intrinsic signal imaging, the peak was negative at 1.13±0.12 s. B6 mice showed a 0.049±0.0081% positive peak in Y-ch at 0.63±0.053s, which seemed to be contamination of flavin signal in Y-ch. No positive peak was detected in C-ch. The peak became 0.044±0.059% (μ/σ ~ 4.8) after ratioing. The eq-ratio signal of Emx1-YC was 1.1±0.071% (μ/σ ~ 12.4). The degree of contamination of eq-ratio signal by flavin signal was estimated to be 3.6% (0.044/1.139) in Emx1-YC mice. I detected negative peaks -0.099±0.014% at 3.33±0.49 s in Y-ch and -0.102±0.017% at 2.93±0.37 s in C-ch. These peaks might correspond to absorption components of the intrinsic signals (Husson et al., 2007, Shibuki et al., 2003). The signals were canceled out with ratioing and became 0.009±0.0021% (μ/σ ~ 0.94) at 2.5 s after stimulation, which was 0.81% (0.009/1.139) of the Emx1-YC eq-ratio signal peak and difficult to distinguish from the noise. I concluded that contamination by flavoprotein and hemodynamic signals was negligible.

Analysis of spontaneous cortical activity and seed-pixel correlation mapping

Spontaneous cortical slow oscillations can reveal interregional functional connectivity even in the absence of direct sensory stimulation (Mohajerani et al., 2013). To assess whether spontaneous slow waves propagate across the entire cortex and show spatially-biased patterns of connectivity, I analyzed intercortical connectivity using seed-pixel correlation mapping. Examples of sequence patterns for spontaneous activity in Emx1-YC and VGAT-YC mice are shown in Figures 5A and 5B. In visual areas, high-amplitude patterns emerged in some frames in Emx1-YC and VGAT-YC, and

other irregular cyclic patterns appeared and disappeared every ~1 s. The frequency spectra of spontaneous activity at each ROI were examined in a range from 0.2 to 2.0 Hz (Figure 5E). The spectral peak of the cortical slow oscillation was between 0.7 and 1.0 Hz. In visual areas, especially V1B, the low-frequency component was predominantly larger than the high-frequency component in the Emx1-YC spectra. This tendency was maintained in visual areas in the VGAT-YC spectra, but was not as large as in Emx1-YC. Low- and high-frequency power components were almost balanced at ROIs of S1BF and S1FL in both genotypes, and at ROIs of S2, A1, and A2D in VGAT-YC. These results suggest that cortical spontaneous activity is not uniform but has a regional bias.

Seed-pixel correlation maps were computed by grand averaging (Emx1-YC, N = 15, n = 8; VGAT-YC, N = 7, n = 5) (Figures 5C and 5D). In Emx1 maps, highly-correlated patterns were divided into: (1) maps of S1BFr and S1FL seeds corresponding to its M1 regions, (2) maps that tracked spread within visual areas, and (3) maps that extend from lateral regions (S2 and A1) to medial regions (M2 and RSD). On the other hand, overall VGAT-YC maps had relatively lower correlations and smaller patterns compared with Emx1-YC maps. Areas in which the correlation coefficient exceeded 0.5 in Emx1-YC maps were significantly larger than those in VGAT-YC maps ($p = 2.80\times10^{-55}$, Wilcoxon rank-sum test) (Figure 5F). Session-pairwise correlations of area patterns with correlation coefficients >0.5 in the same seeds were calculated within the same genotypes and across different genotypes. There were significant differences between all groups (Kruskal-Wallis test, $\chi^2(2, 4848) = 1712$, $p = 0$; Multiple comparison by Dunn's method, within Emx1-YC vs within VGAT-YC, $p = 0$, within Emx1-YC vs across genotypes, $p = 0$, within VGAT-YC vs across genotypes, $p = 7.67\times10^{-19}$) (Figure 5G). The results indicate that patterns of seed-pixel correlation maps between Emx1-YC and VGAT-YC were dissimilar.

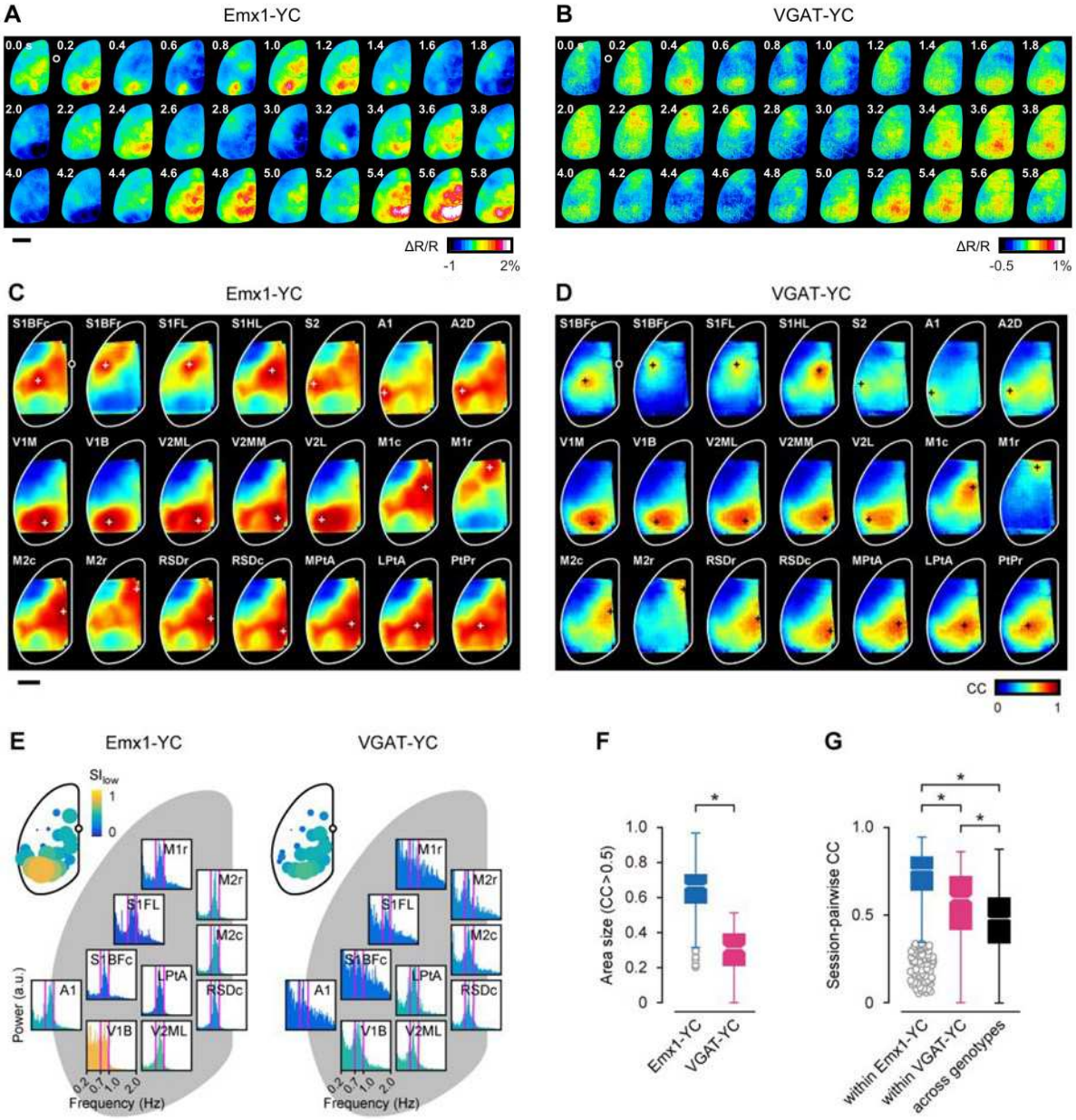

Figure 5
Spontaneous activity and its seed-pixel correlation maps.
(A and B) Sequence patterns of spontaneous activity in Emx1-YC and VGAT-YC mice. Open circles indicate bregma.
(C and D) Seed-pixel correlation maps of spontaneous activity in Emx1-YC and VGAT-YC mice. Cross marks indicate locations of seed pixels at each ROI.
(E) Region specificity of frequency structures in spontaneous activity. Power spectra at representative ROIs are shown at the locations of each ROI in the hemisphere. Magenta vertical lines exhibit frequency ranges from 0.7 to 1.0 Hz. Color codes and bubble sizes indicate superiority of low-frequency component (SI_{low}) in the top-left insets.
(F) Area sizes of correlation maps in which the correlation coefficient exceeded 0.5. Gray open circles indicate outliers.
(G) Session-pairwise correlation coefficients of correlation map patterns in which correlation coefficient exceeded 0.5.

Cross-correlation analysis of spontaneous activity in cortical slow oscillations

To examine the activity relationships between ROIs in more detail, I analyzed cross-correlations of spontaneous activities in all pairwise combinations of ROIs ranging from -1.5 to 1.5 s for multiple sessions (Emx1-YC, N = 15, n = 8; VGAT-YC, N = 7, n = 5) (Figures 6A and 6B). Example cross-correlograms between LPtA and other ROIs are shown in Figure 5C. There were second peaks of the correlations from 1 to 1.5 s of the absolute time lag, indicating that oscillatory components from about 0.7 to 1 Hz in spontaneous activity coincided with cortical slow oscillations. In LPtA vs S1BFc, S1FL, and A1, time lags in the cross-correlograms indicate inward flow of the cortical slow oscillation from these counterpart regions to the node (see also reddish or yellowish links in LPtA panel in Figures 6A and 6B). On the other hand, in LPtA vs V1B, delayed time lags indicated outward flow from the node to the counterparts (see also bluish links in Figures 6A and 6B). In LPtA vs RSDc, the absence of a time lag indicates no net flow between the node and counterparts regions (see also green links in Figures 6A and 6B).

To quantify globally-averaged features of time lags and cross-correlations at each node, I defined “divergence” as an index of the sink and source strength of the flow (Figure 6D, see Chapter 2). The divergence of Emx1-YC mice demonstrated the following tendencies: (1) nodes of S1BFc, S1FL, S2, and M1r had a strong source tendency, (2) visual areas had a strong sink tendency, (3) A1 had a moderate source tendency, and (4) medial/parietal areas, except LPtA, had a no-flow tendency, such as a hub of flows. On the other hand, in VGAT-YC, (1) only S1BFc had a strong source tendency, (2) visual areas had a strong sink tendency, (3) S2 and A2D had a moderate source tendency, and (4) medial/parietal areas had a no-flow tendency. The tendencies observed at S1FL, M1r, and LPtA regions in Emx1-YC were absent in VGAT-YC. I defined a “hub-like index” from the divergence values as high-linked and source/sink-like balanced areas (Figure 6E), resulting medial and parietal areas showed high hub-like index.

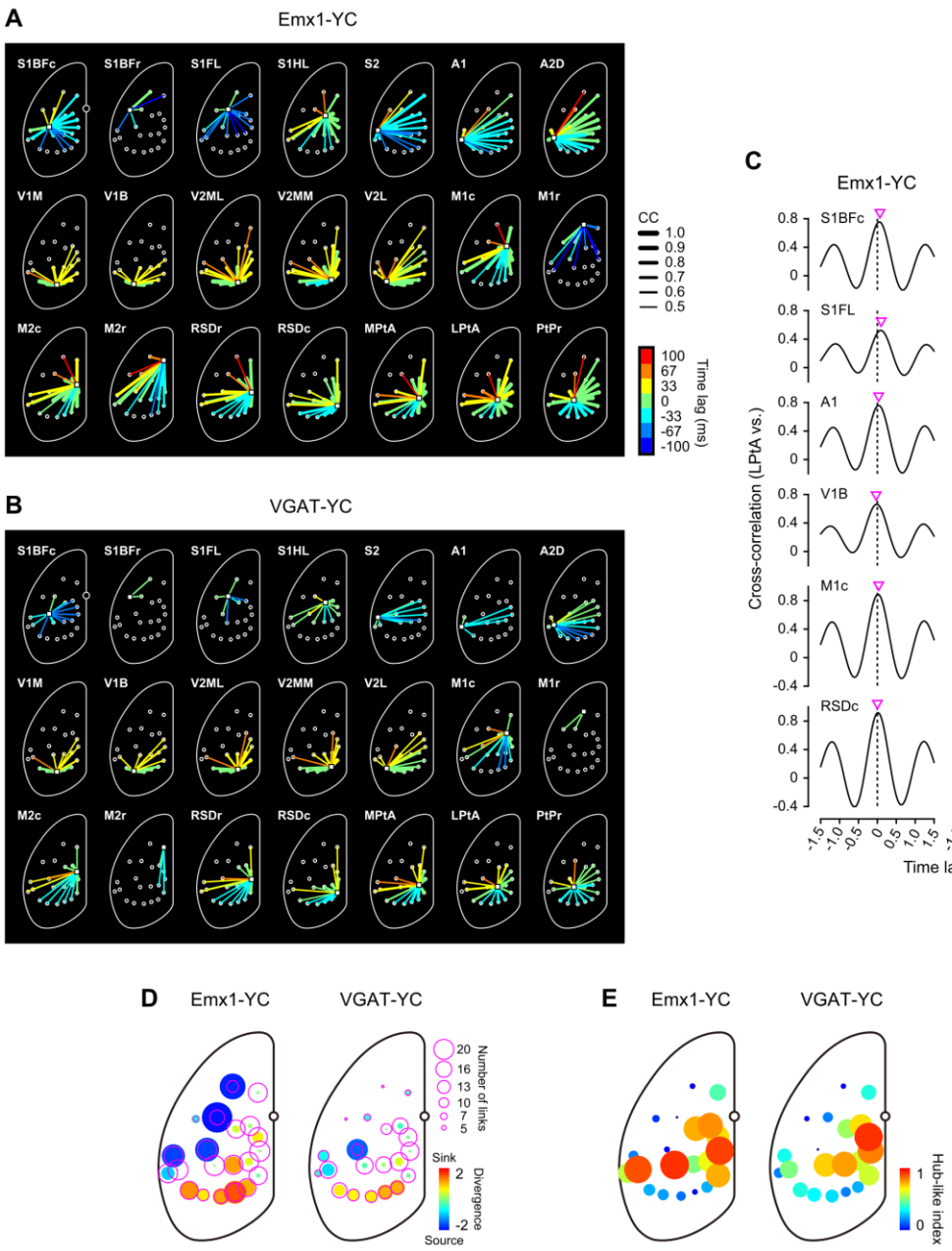

Figure 6
Cross-correlation analysis of spontaneous activity.
(A and B) Cross-correlation diagrams between target ROIs (nodes) and the others. Cross- correlation coefficients at time 0 were turned into widths of the lines. Time lags of crosscorrelations were encoded as pseudo colors. White squares are the nodes.
(C) Cross-correlograms of spontaneous activity between a target node (LPtA) and representative counterpart ROIs. Vertical dotted lines indicate time point 0 and magenta triangles indicate peaks of cross-correlations.
(D) Divergence, an index of time lags and cross-correlations at each node. Bubble color and size indicate the divergence. Values higher and lower than 0 indicate sinks and sources of activity flows, respectively. Value 0 indicates no flow. Magenta open circles indicate the number of links.
(E) Hub-like index, calculated from divergence and the number of links. Bubble color and size indicate the index values.

Cortical parcellation of spontaneous activity

I tested whether spontaneous slow oscillations were parcellated into functional domains by hierarchical clustering (e.g. White et al., 2011). Examples of cortical parcellations that consist of 24 clusters were exhibited in Figures 7A - 7D. Clusters of which parcel numbers or colors are close to each other have similar characteristics of temporal dynamics in the spontaneous activity. Visual areas seems to be extracted stably at the posterior field of the cortex (red areas), and anterior somatosensory and motor areas (blue areas) are always likely to be found in the both genotypes, suggesting that spontaneous activity maintains features of several functional domains regardless of Emx1-YC or VGAT-YC mice. In the example of dendrogram (Figure 7E), clusters were divided into 3 groups, clusters 1 - 9, clusters 22 - 24 and clusters 10 - 21, which represented lateral and anterior parts of somatosensory areas and anterior motor areas, visual areas and the others, respectively. Similar clusters gathered together near in clusters 22 - 24, whereas similar clusters were separated at a distance in clusters 17 and 18, which suggests both short- and long-range connections of cortical networks. Time courses reordered in the parcel orders are shown in Figure 7F, in which the phases of the oscillations in the posterior parts of parcel number greater than around 20 were likely to be shifted from those in the other regions.

To confirm whether and how much clustered areas from spontaneous activity coincided with patterns of sensory-evoked areas, I compared degrees of overlaps between each evoked area and the clustered areas. The same data set for delineating neurometrics was used for representations of each evoked area by averaging over stimulus conditions from the largest intensity to the fourth intensity and grand-averaging (whisker: N = 10, n = 8; auditory, N = 9, n = 7; visual, N = 7, n = 6) (Figure 7G, top). Degrees of overlaps between each evoked area and the clustered areas were turned into an index and the most overlapped clusters were determined (Emx1-YC, N = 15, n = 8; VGAT-YC, N = 7, n = 5) (Figure 7G, middle and bottom). Centroids of the selected clusters were plotted in Figure 7H, in which the centroids were localized around the center of each evoked area. The area sizes of selected clusters were relatively small in the whisker and auditory stimulus

conditions, whereas large in the visual stimulus condition, except the secondary auditory evoked area in Emx1-YC, in both genotypes (Emx1-YC, $\chi^2(3, 56) = 37.4$, $p = 3.87\times10^{-8}$; VGAT-YC, $\chi^2(3, 20) = 10.3$, $p = 0.0160$, Kruskal-Wallis test, Dunn's method for multiple comparison) (Figure 7I). The overlap indices were higher in visual and primary-auditory evoked areas than the others in Emx1-YC, whereas relatively higher in visual evoked areas in VGAT-YC (Emx1-YC, $\chi^2(3, 56) = 29.6$, $p = 1.65\times10^{-6}$; VGAT-YC, $\chi^2(3, 20) = 8.89$, $p = 0.0308$, the same methods as the area size) (Figure 7J). These data strongly suggest that spontaneous slow oscillation represents functional cortical domain structures. Comparing to optical intrinsic imaging (White et al., 2011), I found that the domains were separated into smaller pieces. These discrepancies of resolution of functional domains parcellated, the number and size of clusters, may come from difference of signal origins between intrinsic signal and calcium signal corresponding to hemodynamics and direct neural activity, respectively, rather than methodological difference of the clustering.

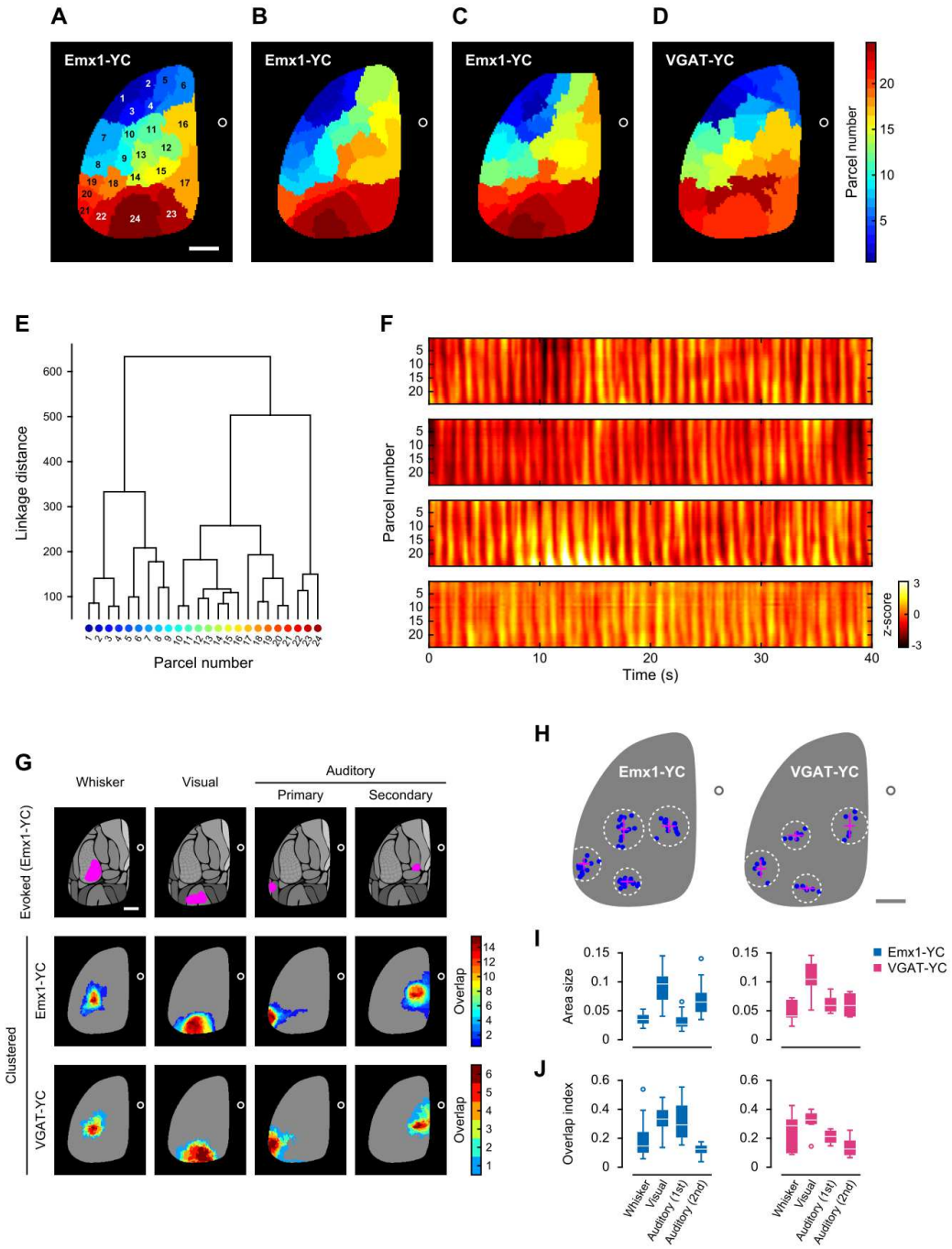

Figure 7
Cortical parcellation of spontaneous activity.
(A - C) Examples of cortical parcellation maps in Emx1-YC mice. Color bar indicate parcel number of clusters and the actual numbers are shown on the map of (A). White open circles indicate bregma. Scale bar shows 1 mm.
(D) An example of the parcellation map in VGAT-YC mouse.
(E) Dendrogram of clustering corresponding to the map of (A).
(F) Color charts of time courses pixel-averaged within each parcel of the parcellation maps, which correspond to the maps of (A) - (D) from the top.
(G) Comparison of evoked responses and clustered areas. Color bars indicate the number of overlaps of clustered areas that were the most similar to each evoked area in several sessions. Scale bar shows 1 mm.
(H) Distributions of centroids of the selected clustered areas (blue dots). Dotted circles encompassed the individual distributions. Magenta crosses exhibit SDs and the centers of the distributions in the cortical field. Gray open circles indicate bregma. Scale bar shows 1 mm.
(I) Area sizes of the selected clustered areas. Open circles indicate outliers.
(J) Overlap index, how much overlapped the selected clustered areas were with each evoked area.

Chapter 4 Analysis of multisensory responses (Kuroki et al., 2018)

Measurement and analysis of multisensory response dynamics across cortex

I next measured cortical response dynamics during MSI in excitatory and inhibitory networks. In a previous study using electrophysiologic methods, multisensory responses showed super- or sub-additivity (Stein and Stanford, 2008). They also found that additivity depends on stimulus-onset asynchrony (SOA) (Wallace et al., 2004). Particularly for visual responses, the additive effect is maximized when the onset of the visual stimulus precedes that of other stimuli by 30–50 ms because of intrinsic delays in the visual responsiveness of V1 (Mohajerani et al., 2013; Wallace et al., 2004). I tested whether multisensory responses based on calcium signals also showed super- or sub-additivity and whether the additivity was influenced by an adjustment of SOAs, by giving visual stimulation simultaneously with (condition V) or 30-ms before (condition Vp) other stimuli. Amplitude responses to each single and multiple stimulus condition are illustrated in all ROIs (Emx1-YC, N = 28, n = 21; VGAT-YC, N = 7, n = 5; Figures 8A and 8B). Response maps to each stimulus captured the spatial extent of the responses to each stimulus, which were similar between genotypes (Early, $p = 0.886$; Late, $p = 0.516$, paired t-test; Figure 8C). The supra-additivity were observed in the excitatory population of the high hub-like index areas ($p = 0.028$, Student's t-test), but not in the inhibitory population ($p = 0.657$, Student's t-test; Figure 8D). The differential responses of excitatory and inhibitory networks were analogous to observations made using electrophysiologic methods in a previous report (Olcese et al., 2013).

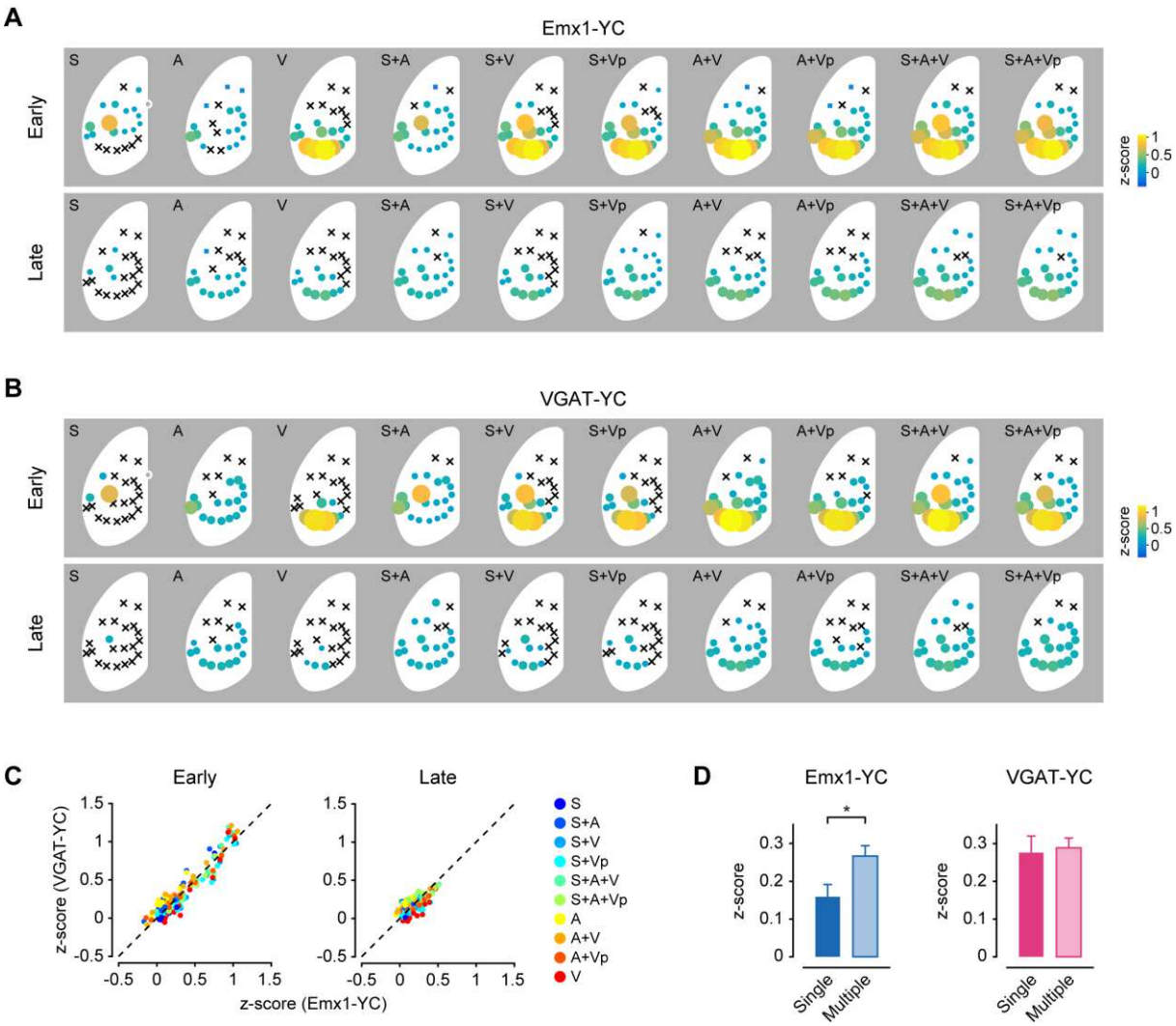

Figure 8

Cortical patterns of multisensory evoked responses.

(A and B) Spatial extents of multisensory responses. Pseudo color and bubble size indicate z-score means of Δ*R*/*R* in response periods. X indicates no significance, the significance level is $p < 0.05$, between baseline and evoked. Early: 0–2 s and Late: 2–4 s after stimulus onset. White open circles indicate bregma.

(C) Scatter plot of the evoked responses for Emx1-YC vs VGAT-YC mice. Dashed lines represent slope = 1 (indicating equivalent z-scores of Emx1-YC and VGAT-YC mice).

(D) z-score of single and multisensory conditions in high hub-like index areas (> 0.5, Figure 6E).

Multisensory responses in the primary sensory areas

I analyzed evoked responses to single-sensory and multisensory stimuli at each primary sensory area in the both genotypes in which response period and pre-stimulus period were determined as

1-s duration after stimulus onset and 5-s duration before stimulus onset, respectively (Emx1-YC, N = 9, n = 7; VGAT-YC, N = 6, n = 4) (Figure 9A). Responses to stimulus combinations of multisensory conditions that included single-sensory stimuli corresponding to each primary sensory area were markedly increased from the baselines in both genotypes (as shown by asterisks, Figure 9A). In contrast, responses significantly increased even in multiple stimulus conditions that did not include corresponding stimuli to each primary sensory area in both genotypes, except in whisker 'S' condition at V1B in VGAT-YC. Responses to each primary single-stimulus conditions and the others demonstrated as following patterns: (1) responses to the other conditions were larger than the primary single condition, (2) smaller than the single condition, and (3) equal to the single condition, of which tendency was different in genotypes (as shown by colored daggers, Figure 9A).

At S1BFc, stimulus combinations including 'S' stimulus generated responses comparable to the response to 'S' stimulus only in the both genotypes. Additionally, 'Vp' stimulus affected to reduce the multimodal responses significantly in Emx1-YC, whereas 'V' stimulus enhanced that in VGAT-YC. The aim of this adjustment is to align the timing of evoked responses delivered to each primary cortex because only visual response is delayed about from 30 to 50 ms compared with the other responses (Mohajerani et al., 2013; Wallace et al., 2004). Cross-modal responses also occurred to stimuli not including 'S' stimulus in the both genotypes. At A1, as the same as responses in S1, large responses were evoked by stimulus combination including 'A' stimulus in the both genotypes, but in Emx1-YC, visual stimulus increased the multisensory responses significantly in the auditory cortex. Cross-modal responses to 'S' and 'V' stimuli were also occurred. At V1B, similarly, multimodal stimuli including 'V' or 'Vp' stimulus induced large responses in the both genotypes. In Emx1-YC, A+V or A+Vp stimulus enhanced responses at V1, whereas S+V or S+Vp stimulus suppressed responses significantly. Response to S+A+V or S+A+Vp stimulus was comparable to single modal responses. In VGAT-YC, S+V, S+A+V and S+A+Vp conditions were different from that of Emx1-YC. SNRs at each ROI in the both genotypes were mostly comparable to each other under multisensory stimulus conditions (Figure 9B). The additivity patterns were complex and

unmatched with previous reports (Stein and Stanford, 2008; Wallace et al., 2004). These discrepancies may depend on experimental conditions, i.e. anesthesia, strain, physiological signal observed, etc. Especially, stimulus duration may be the greatest influence on the discrepancies between my results and theirs; the duration was 500 ms in the current study, and up to 50 ms in the previous studies. For physiological signals, membrane potential and calcium ion dynamics are not precisely synchronized, however they should be macroscopically proportional, because of their distinct molecular mechanisms (Grienberger and Konnerth, 2012). Furthermore, although excitatory and inhibitory synaptic inputs are balanced under anesthetized state, the balance shifts toward inhibitory in awake (Haider et al., 2013).

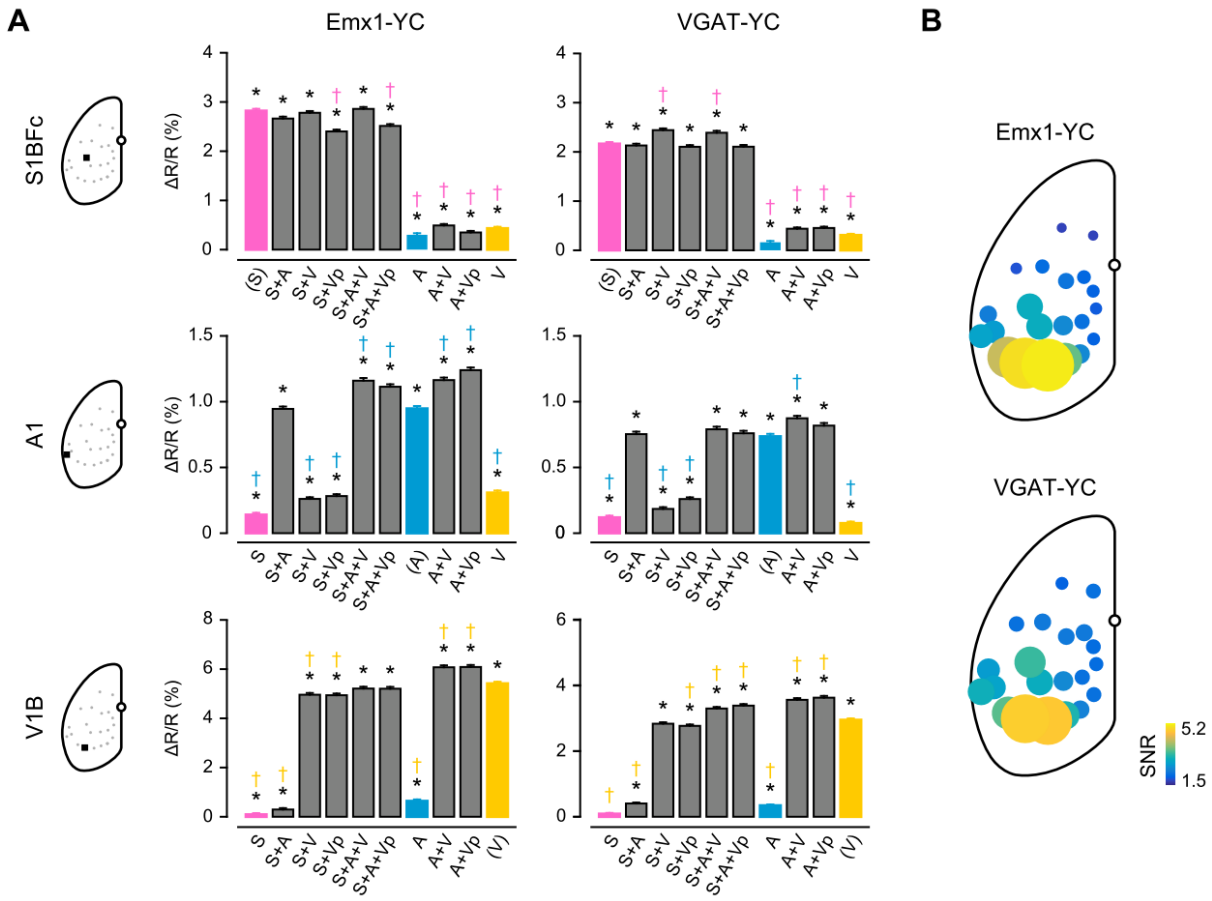

Figure 9
Multisensory responses in the primary sensory areas.
(A) Evoked responses to single and multiple sensory stimuli at primary sensory areas in Emx1-YC and VGAT-YC mice. Asterisks indicate significance between baseline and evoked responses. Daggers represent significant differences between primary responses and the other stimulus conditions. The significance level is p = 0.001. Single stimulus conditions in parenthesis show the primary responses. S: somatosensory whisker stimulus, A: auditory stimulus, V: visual stimulus, Vp: preceded visual stimulus. Black squares in schematics of the left hemisphere indicate the primary sensory areas. Open circles show bregma. Error bars indicate S.E.M.
(B) Signal-to-noise ratios across all stimulus conditions in the all ROIs.

Phase-locking of slow waves by multisensory inputs in cortical hub areas

I examined whether phase responses at association areas or boundary regions could be modulated by multisensory inputs. Averaged time traces for single and multiple stimulus conditions at example ROIs are shown in Figure 10A. In S1 area, large evoked responses to multimodal stimuli including the 'S' stimulus were generated prominently in both genotypes. In M2c and PtPR areas during the S, S+A, and S+A+V stimulus conditions, cortical slow-oscillation components persisted in the post-stimulus period (Figure 10A, closed arrowheads) compared with the pre-stimulus period (Figure 10A, open arrowheads) regardless of averaging, indicating that ongoing cortical slow oscillations were phase-locked, defined that phasic oscillations of a ROI were aligned for seconds among trials.

To quantify the phase-locking, I determined the phase-locking factor (PLF) (Kawasaki et al., 2014; see Chapter 2). In the Emx1-YC, phase-locking occurred globally under the A, S+A, A+V, S+Vp, S+A+V, and S+A+Vp stimulus conditions, particularly in the primary sensory and medial regions (N = 28, n = 21; Figure 10B, Early). The phase-locking lasted for ~4 s after stimulation offset in the medial regions under the S, S+A, and S+A+V conditions (Figure 10B, Late). The VGAT-YC also showed phase-locking in the early time window (N = 7, n = 5; Figure 10C), but the degree of phase-locking was significantly lower than that in Emx1-YC ($p = 2.26 \times 10^{-23}$, paired t-test; Figure 10D), despite the absence of a difference in the evoked responses (Figure 8C). The degrees of PLF in the high hub-like index areas were enhanced by a multisensory stimulus in Emx1-YC ($p = 2.88 \times 10^{-5}$, Student's t-test), but not in VGAT-YC ($p = 0.447$, Student's t-test; Figure 10E). I also observed a stimulus-intensity dependence of phase-locking in each sensory modality (Figure 11). The stimulus-intensity dependency, however, was much smaller than the degree of multisensory phase-locking.

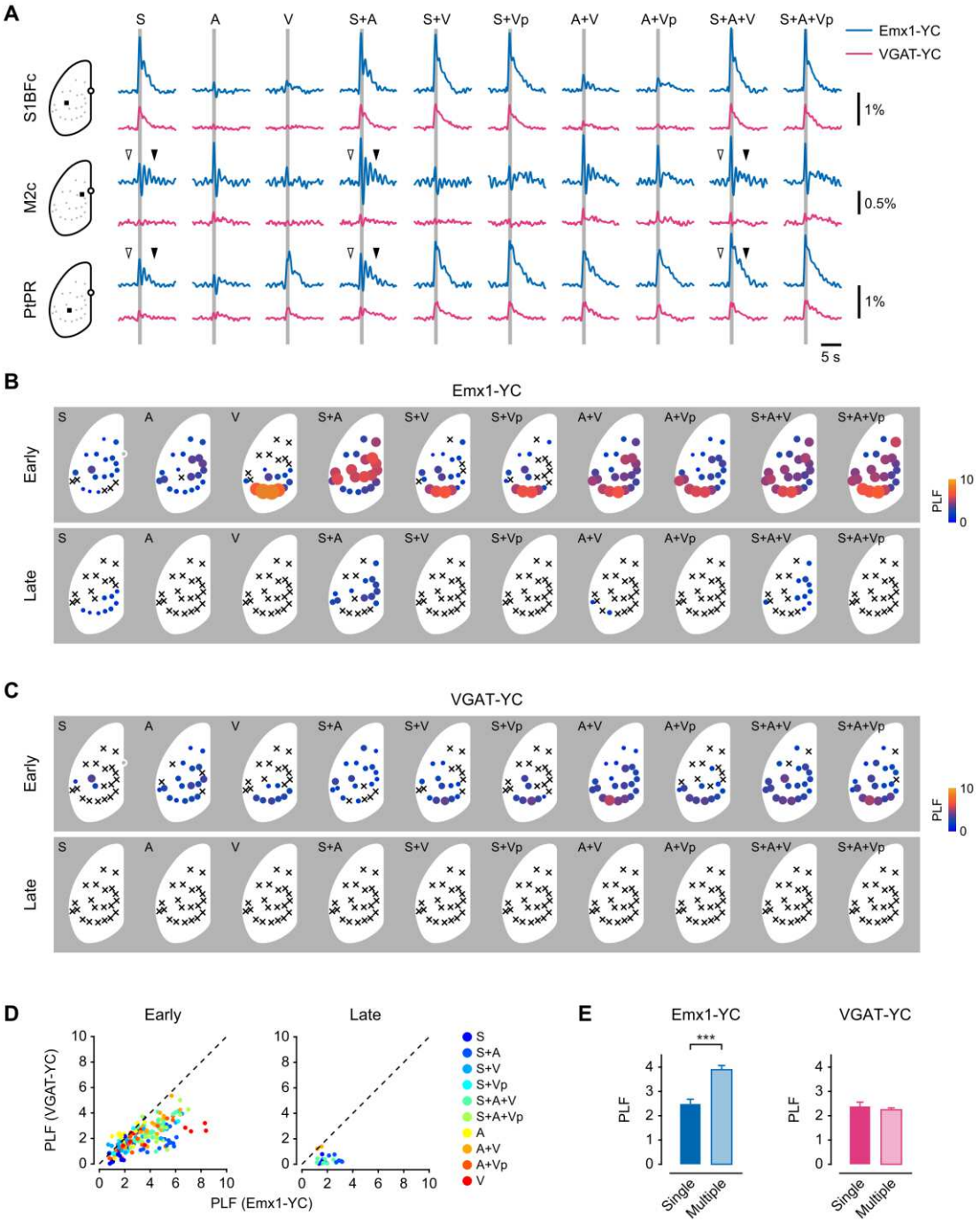

Figure 10
Multisensory inputs induce phase-locking of cortical slow wave activity
(A) Grand-averaged time traces in single and multiple stimulus conditions at example ROIs. Gray hatches indicate 500-ms stimulus period. Stimulus conditions are shown above the gray hatches. Open and closed arrowheads exhibit traces at pre- and post-stimulus periods, respectively, at M2c and PtPR under the S, S+A and S+A+V stimulus condition.
(B and C) Phase-locking factor maps of single and multiple stimulus conditions. Pseudo color and bubble size show the phase-locking factor. X indicates no significance, the significance level is $p < 0.05$, from pre-stimulus baseline. Early: 0–2 s and Late: 2–4 s after stimulus onset. White open circles indicate bregma. PLF: phase-locking factor.
(D) Scatter plot of the PLF for Emx1-YC vs VGAT-YC mice. Dashed lines represent slope = 1 (indicating equivalent PLFs of Emx1-YC and VGAT-YC mice).
(E) PLF of single and multisensory conditions in high hub-like index areas (> 0.5, Figure 6E).

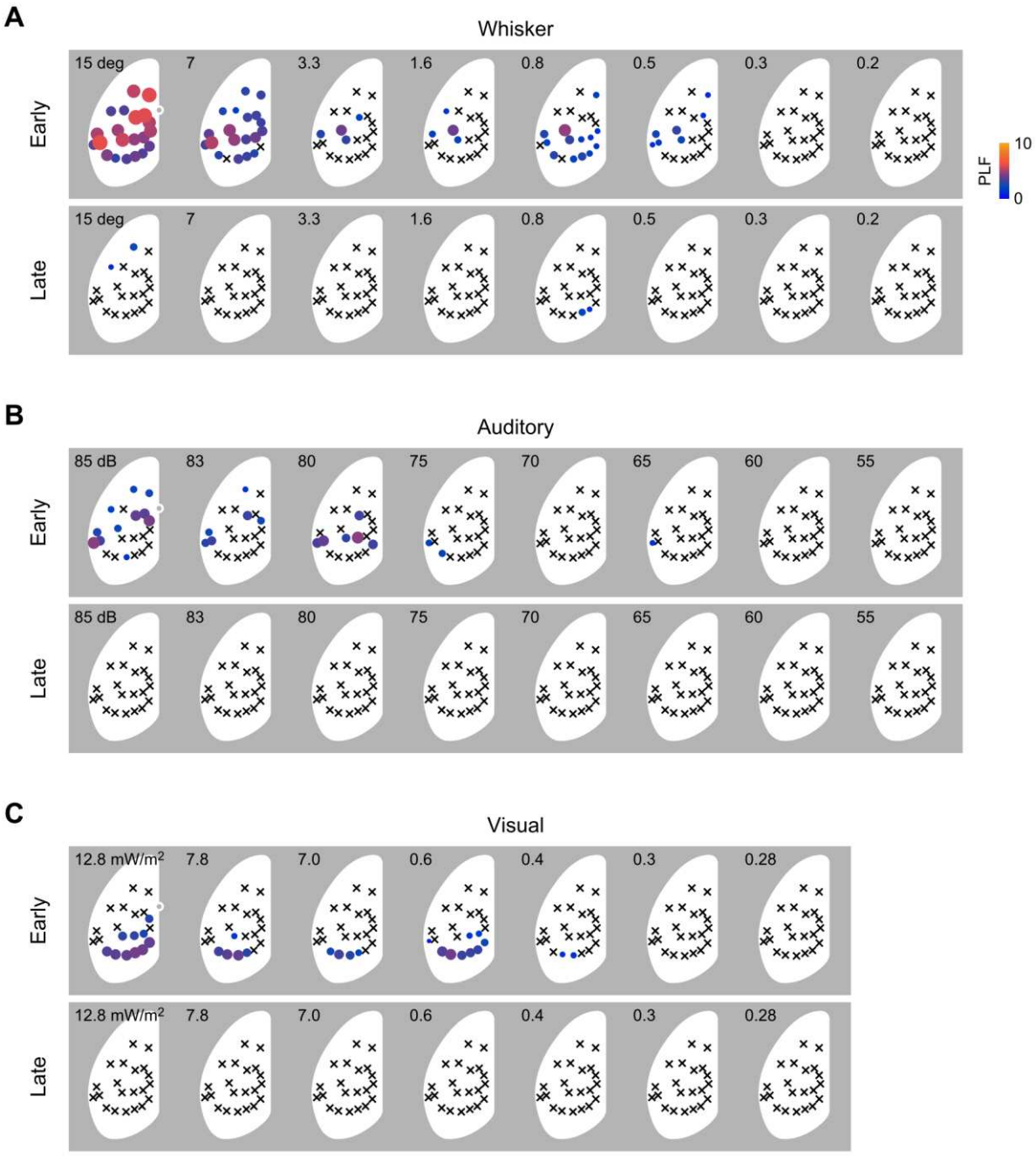

Figure 11
Stimulus-intensity dependency of phase-locking
(A – C) Phase-locking factor maps of single stimulus conditions for whisker, auditory and visual stimuli in Emx1-YC mice. Stimulus intensities were altered the same as in Figures 3G and 3H. Pseudo color and bubble size show the phase-locking factor. X indicates no significance, the significance level is $p < 0.05$, from pre-stimulus baseline. Early: 0–2 s and Late: 2–4 s after stimulus onset. White open circles indicate bregma.

To gain insight into the cause of the phase-locking phenomena, I carried out the following experiments. The PLF patterns suggested that multisensory signals converge in the association areas and modulate neuronal activities of cells in the areas as a function of multimodal integration.

Population calcium signals, however, may represent either postsynaptic cells or presynaptic terminals. To reveal the phase-locking of postsynaptic cells in those areas, I injected AAV-DJ/8-CaMKIIα-Cre (AAV-CaMKIIα-Cre) locally into the medial cortical area of tLSL-YC2.60 Tg mice. The mice expressed YC2.60 only in the medial cortex. Phase-locking was induced in these areas in these mice (N = 12, n = 6; Figures 12A and 12B), indicating that the phase-locking occurred precisely in the medial cortical neurons. I also injected viruses into the S1BFc and analyzed the whisker evoked responses. The mice showed the evoked response in the S1BFc, but did not show in the primary and secondary motor areas although Emx1-YC showed the response with the same condition, indicating the calcium signals scarcely contained axonal activities at the projecting sites (N = 3, n = 3; Figures 12C and 12D). To test whether direct excitatory inputs from primary sensory areas to association areas control the phase-locking, I measured the PLF in Emx1-YC under pharmacologic inactivation of the S1 area by muscimol, a $GABA_A$ receptor agonist. I originally hypothesized that PLF of the association areas would be decreased by silencing the S1 area. In contrast to my initial assumption, however, the PLF was significantly increased by S1 inactivation (N = 7, n = 7; Early, $p = 1.12\times10^{-21}$; Late, $p = 2.06\times10^{-6}$, paired t-test; Figure 13A and 13D), though evoked responses and PLF at the S1 were suppressed, as expected (z-score, $p = 1.46\times10^{-8}$; PLF, p = 0.0337, Wilcoxon rank-sum test; Figures 13B and 13C). The PLF of Emx1-YC mice was also calculated under the awake and the isoflurane-anesthetized conditions (awake, N = 10, n = 6; isoflurane-anesthetized, N = 8, n = 8; Figure 14E and 14F). The PLF was still observed in both conditions. In the isoflurane-anesthetized condition, the PLF in the medial areas was largely diminished, probably reflecting the difference in slow-wave flow under this condition (Figures 6D, 14B and 14D). Spontaneous functional connections were consistent among all states (Figures 14A and 14C). These results suggest that neuronal activities of primary sensory areas are relayed polysynaptically to medial association areas and induce phase-locking in these areas.

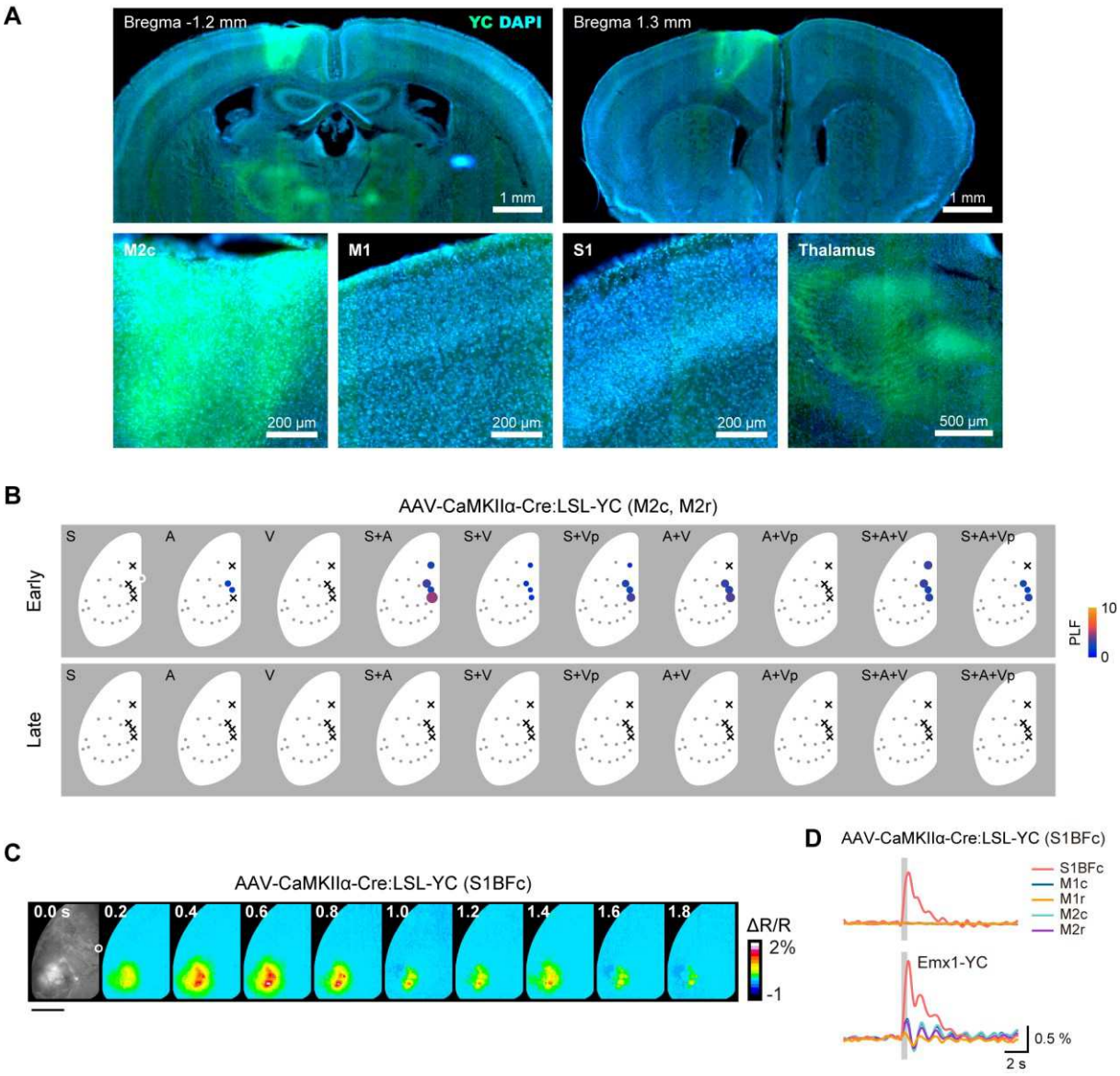

Figure 12
Phase-locking induced by multisensory inputs occurs postsynaptically.
(A) Fluorescence images of AAV-Cre locally-injected (in the M2r and M2c) tLSL-YC2.60 Tg mice. Upper panels show low-magnification images. Upper left and right panels show coronal images at areas M2c and M2r, respectively. Lower panels show high-magnification images at M2c, M1, S1, and thalamus.
(B) Phase-locking factor maps of single and multiple stimulus conditions of the AAV-Cre locally-injected tLSL-YC2.60 Tg mice. Pseudo color and bubble size show the PLF. X indicates no significance, the significance level is $p < 0.05$, from pre-stimulus baseline. Early: 0–2 s and Late: 2–4 s after stimulus onset. White open circle indicates bregma.
(C) Image montage of evoked responses to whisker stimuli in AAV-Cre locally-injected (in the S1BFc) tLSL-YC2.60 Tg mice. The first frame shows a cortical yellow image through the skull. Open circle indicates bregma. Scale bar = 2 mm.
(D) Averaged time-courses of sensory responses to whisker stimuli at ROIs of S1BFc, M1c, M1r, M2c, and M2r in AAV-Cre locally-injected (in the S1BFc) tLSL-YC and Emx1-YC mice. Gray bars show the sensory stimulation period.

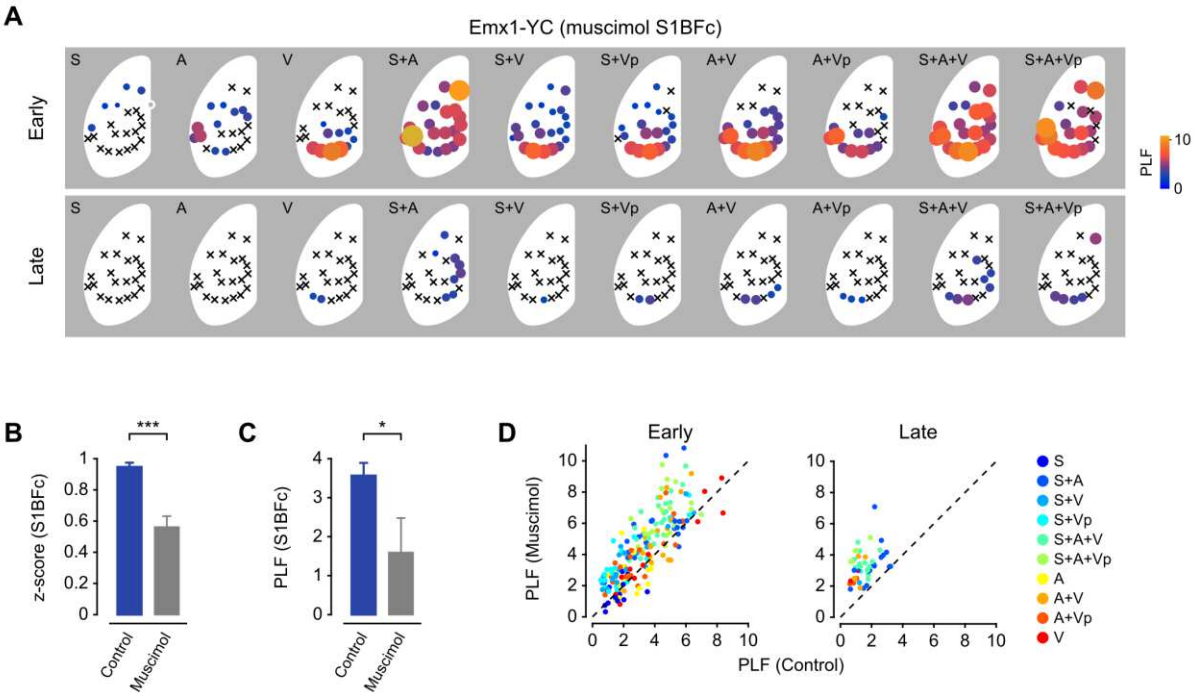

Figure 13
S1 inactivation facilitates phase-locking
(A) Phase-locking factor maps of single and multiple stimulus conditions of Emx1-YC mice after muscimol injection in the S1BFc. Pseudo color and bubble size show the phase-locking factor. X indicates no significance, the significance level is $p < 0.05$, from pre-stimulus baseline. Early: 0–2 s and Late: 2–4 s after stimulus onset. White open circle indicates bregma.
(B) Evoked early response in the S1BFc area to S stimulation.
(C) Early PLF in the S1BFc area with S stimulation.
(D) Scatter plot of the PLF for muscimol inactivation vs control. Dashed lines indicate slope = 1 (PLFs of muscimol inactivation and control are equal).

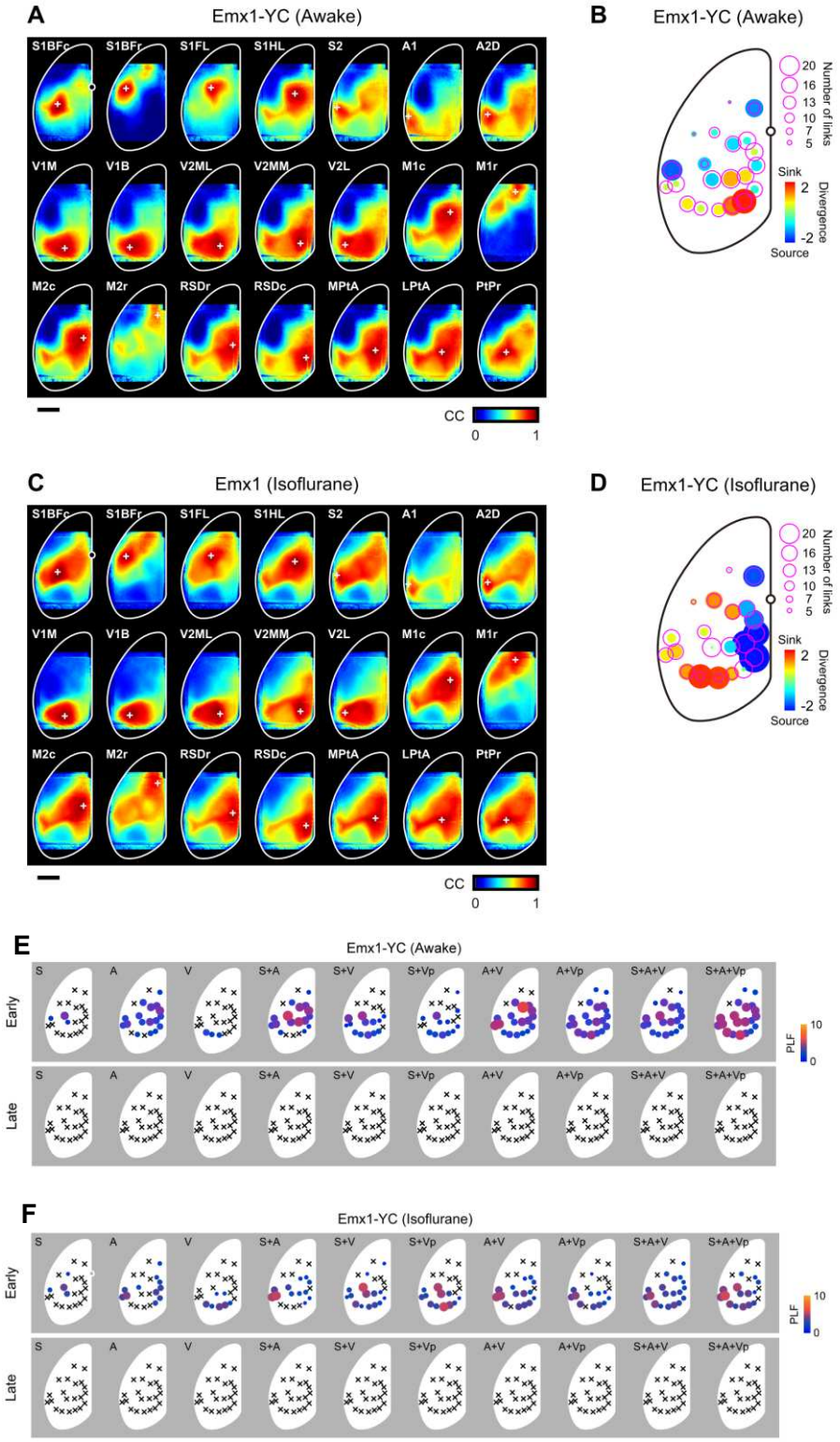

Figure 14
Phase-locking under awake and isoflurane-anesthetized state.
(A and B) Seed-pixel correlation maps (A) and divergence index and link number (B) in the awake state.
(C and D) Seed-pixel correlation maps (C) and divergence index and link number (D) in isoflurane-anesthetized state.
(E and F) Phase-locking factor maps of single and multiple stimulus conditions of Emx1-YC mice under (E) awake and (F) isoflurane-anesthetized conditions. Pseudo color and bubble size show the phase-locking factor. X indicates no significance; the significance level is $p < 0.05$ from pre-stimulus baseline. Early: 0–2 s and Late: 2–4 s after stimulus onset. White open circle indicates bregma.

Chapter 5 Discussion

In this study, I addressed several long-standing questions on the cortical dynamics of MSI. To study these issues I engineered a Tg mouse line to report wide-field, cell-type-specific, cortical calcium activity and analyze the data with novel data visualization tools. I demonstrate high resolution imaging of spontaneous cortical slow waves and their modulation by sensory stimulation from visual, auditory, and somatosensory modes, individually and in combination. Remarkably, even in the absence of stimulation, I observed structured connectivity in cortical slow wave dynamics, with a prominent hub-like architecture in medial/parietal association areas. The observed hubs were evident for excitatory and inhibitory networks, had balanced source/sink inputs, and during multisensory inputs the excitatory network showed prominent phase-locking of slow waves persisting for several seconds beyond the stimuli indicating signal integration, while the inhibitory network served network synchrony in a non-phase locking support role. Collectively, these findings reveal the spatial and temporal preconditions and cortical physiological states under which cross-modal interactions occur suggesting new principles of MSI.

Calcium signals of Tg mice accurately reflect neuronal population activity

Population calcium signals could originate from the soma and neuropil/axons (Grienberger et al., 2012) that correspond to neuronal inputs and outputs, respectively, and are correlated (Kerr et al., 2005). Despite the complexity of possible subcellular sources of calcium signals, experiments with mice locally expressing YC2.60 revealed that calcium signals in my conditions represented well neuronal activities at the selected sites but not remote-projection sites (Figure 12). Consistently, calcium signals of excitatory populations correlated well with local field potential signals and multiunit activities at the sites monitored (Figure 4). There were close correlations between the z-scores of Emx1-YC and VGAT-YC mice upon multisensory evoked responses (Figure 8C). These data suggest that the calcium signals detected in the wide-field imaging condition largely represent

activities of cells in local fields. Spontaneous and evoked responses in my wide-field imaging at a high sampling rate demonstrated information flows in broad cortical areas.

Although the input excitatory and inhibitory synaptic conductances in neurons are balanced (Haider et al., 2006; Okun and Lampl, 2008) and the output membrane potentials of adjacent excitatory and inhibitory neurons are roughly synchronized (Neske et al., 2015), in my data analyzed from Emx1-YC and VGAT-YC mice, I observed the dissimilarity in the seed-pixel correlation maps (Figures 5C−5F), cross-correlation features (Figure 6D), and phase-locking by multisensory stimuli (Figures 10B and 10C). I need more sophisticated researches to reveal what make these differences while it must reflect differences between excitatory and inhibitory networks in anatomy and physiology (e.g. Tamamaki and Tomioka, 2010; Haider et al., 2013).

Comparison with other indicators and Tg mouse lines

There are several Tg mice lines, which express genetic encoded calcium or voltage indicator in cell-specific manner (Madisen et al., 2015; Zariwala et al., 2013). Comparing YCs and GCaMPs, YCs, especially YC2.60 and YC nanos, shows high affinity to calcium and high noise immunity (Horikawa et al., 2010), which indicate YCs can detect low concentration calcium dynamics such as sub threshold activity. On the other hand, GCaMPs shows fast kinetics and large fluctuation (Chen et al., 2013), but low calcium affinity and hard to apply noise canceling method of FRET-based sensors because the GCaMPs are single fluorescence protein-based. Large fluctuation of fluorescence signal can overcome the low noise immunity and actually tLSL-YC2.60 and GCaMP3 Tg mice crossed with Emx1-Cre showed similar SNR for wide-field calcium imaging (Vanni and Murphy, 2014). Properties of genetically encoded voltage sensors were improved recently and it can be applied in vivo experiments and can detect high frequency (> 50 Hz) action potentials (Akemann et al., 2012; Midisen et al., 2015; Tsutsui et al., 2013). However, it is still hard to detect the signals compared to calcium indicators, because of expression site of the sensors and range of signal fluctuations. Voltage probes should be reside the cell membrane because

membrane potential can be detected only there while calcium fluctuation can be detected in cytosol, and the ranges of voltage fluctuation is much smaller than those of calcium signals (Knöpfel, 2012). We can localize the sensors at specific site in a cell (e.g. Akerboom et al., 2012) or detect other type signals (Lin and Schnitzer, 2016) by fusing or exchanging with other protein. Tg mice containing these sensors can improve S/N ratio of signals or show signal processing of sub-neuronal domains such as dendritic branch, axon, spine, bouton, axon hillock and a specific signal input sites (e.g. near dopaminergic receptors).

Spontaneous and evoked slow waves self-organize into cortical pathways and hubs

My recordings in the absence of sensory stimulation demonstrate that brain-wide spontaneous slow wave activity was patterned into hub-like structures presumably representing functional connectivity in defined neural circuits. Previous studies suggest that specific sensory response patterns are reflected in spontaneous activity (Kenet et al., 2003; Saitoh et al., 2010), which can be extracted by seed-pixel correlation analysis (Farley and Noreña, 2013; Yoshida et al., 2008) to assess global connectivity in the cortex (Mohajerani et al., 2013). In my seed-pixel correlation maps of the excitatory neuronal network (Figure 5C), highly-correlated patterns in somatosensory cortex (Aronoff et al., 2010; Manita et al., 2015), visual cortex (Wang et al., 2012) and auditory cortex closely aligned with known functional anatomical connections (Mohajerani et al., 2013). Strong auditory responses emerged around parietal areas (Figure 3A) and the seed-pixel correlation maps suggest connections between auditory and parietal areas (Figure 5C). Parietal areas have connections with A2D, RSD, S1, M1/M2, and cingulate cortex (Wilber et al., 2015), which may contribute to the resemblance between correlation map patterns where seeds were located in auditory, M1, M2, RSD, and parietal areas. Slow waves propagating from each primary sensory area to the entire cortex passed through the medial/parietal areas and terminated at PtA (in case of S1 and A1 origins) and at M2 (in case of V1 origin) areas within ~20 ms from the rise of each evoked response (Mohajerani et al., 2013). My results are consistent with response patterns

evoked by artificial cortical microstimulation (Hishida et al., 2014; Lim et al., 2012), suggesting direct and polysynaptic projections between these cortical pathways. Taken together, spontaneously correlated cortical maps exhibited static connectivity between sensory areas and medial/parietal areas presumably derived from direct and polysynaptic connections.

I expected not only connections but also functional domains and the borders (Figures 7A-7D) from the spontaneous time course changes of slow waves. The spatial patterns, especially representing primary sensory areas, were overlapped with sensory evoked patterns (Figures 7G-7J). Regional bias displayed as frequency structures of the slow oscillation (Figure 5E) may be reflected as the functional domains. Low-frequency superiority, dominancy of low-frequency component over high-frequency component of cortical slow waves in V1 was the highest in the excitatory network consistent with a prolonged down state duration in V1 (Chauvette et al., 2011). Region-specific differences in the form of long-range projections may derive from differences in cortico-cortical, thalamo-cortical, and transcallosal connections. Slow wave flow generates starting and ending points in every part of the cortex (McCormick et al., 2015), and, in particular, wave flow may not be able to pass easily through the boundaries of certain areas, such as the borders of V1 (Xu et al., 2007) compared with other areas, as I showed highly-correlated patterns exclusively in V1 (Figure 5C). Moreover, although visual areas had a higher probability of being sinks than other areas (Figure 6D), V1 had a relatively small divergence, sink/source strength of cortical flows, compared with V2. These results suggest that a lower occurrence of slow waves can result from their low-frequency superiority.

In the excitatory network, the most anterior ROIs had delayed time-lag links, whereas the posterior ROIs had preceded time-lag links dominantly (Figure 6A). These results indicate that the phase of slow oscillation in the anterior part precedes the phase in the posterior part, suggesting an anterior to posterior wave flow (Sheroziya and Timofeev, 2014; Stroh et al., 2013; Vyazovskiy et al., 2009). I also estimated the slow wave velocity be 20–40 mm/s, which roughly agrees with previous *in vivo* studies using ketamine/xylazine anesthesia (Fucke et al., 2011; Luczak et al.,

2007; Sheroziya and Timofeev, 2014; Stroh et al., 2013). For divergence of the wave flow at each ROI (Figure 6D, left), the locations of ROIs corresponded to those identified in previous reports (Hishida et al., 2014; Lim et al., 2012; Zingg et al., 2014). My finding is that functional connectivity like hub structures was detected even in spontaneous activity without direct probing techniques such as micro-circuit stimulation or labeling circuitry.

It is likely that the late components of sensory-evoked responses derive from the reverberation of neural activity at the following three functional neural connections: (1) intracortical (Chen et al., 2015; Funayama et al., 2015; Grienberger et al., 2012), (2) cortico-thalamo-cortical (Lee and Sherman, 2010; Stroh et al., 2013; Theyel et al., 2010), and (3) transcallosal (Mohajerani et al., 2010; Petreanu et al., 2007) ones. Distinct peak patterns might represent characteristic reverberation circuits in different sensory areas (Figure 3E). The reverberating activity was prominently observed, particularly in auditory response, in which an increase in the activity, even in visual areas, persisted for ~1.5 s to several seconds after the early response at the parietal area (Figures 3A and 3B). This result may be based on strong reverberations in reciprocal connections among auditory, parietal, and visual areas. An auditory stimulus is frequently used as an alert cue (e.g., Manly et al., 2002). This may be because cortex-wide networks underlying the reverberations may increase awareness by auditory cues.

Phase-locking of spontaneous slow waves in cortical hubs during multisensory input

Phase synchronization is referred to as the entrainment of the oscillatory phases between distinct brain areas and may contribute to the communication and association of interregional information with mainly theta and gamma oscillations (Fell and Axmacher, 2011). Intercortical phase synchronization also occurs in slow oscillations at the delta-wave frequency during a multimodal association task (Weiss and Rappelsberger, 2000) and a working memory task (Fujisawa and Buzsáki, 2011). Furthermore, slow oscillations modulate amplitudes of faster oscillations, referred to as cross-frequency coupling (Aru et al., 2015), which may influence phase synchronization in

faster oscillations. My findings indicate that medial/parietal cortices form hubs for information transmission and are likely important for MSI and sensory-motor association (e.g., Harvey et al., 2012; Makino and Komiyama, 2015; Makino et al., 2017; Robinson et al., 2011; Yoshitake et al., 2013). Local phase-locking, if expanded to the entire cortex induced by multisensory stimuli, may represent a neural substrate underlying MSI elicited by intercortical phase synchronization.

Distinct from phase-locking, phase-resetting is a phenomenon where the phase of sensory responses aligns between trials in primary sensory areas and lasts within several hundred milliseconds (Kayser et al., 2008; Lakatos et al., 2007; Sieben et al., 2013). My results are consistent with these studies showing that multisensory stimulation produces stronger phase-resetting than single sensory stimulation (Figure 10B). Phase-resetting is suggested to be induced by interactions between different sensory thalamic areas and between primary cortical areas (Lakatos et al., 2007; Sieben et al., 2013). Depending on the sound-stimulus rhythm attended by a monkey, membrane potentials oscillate persistently for several seconds in the auditory cortex (Lakatos et al., 2013). The authors suggested the modulation of cortical activity by non-specific thalamic nuclei controlled by directed attention. The previously mentioned corticothalamic reverberations in phase-resetting (Lee and Sherman, 2010; Stroh et al., 2013) may also contribute to long-lasting phase-locking. Consistent with this notion, the data obtained under silencing of the primary sensory area (S1) suggest that polysynaptic mechanisms underlie the phase-locking (Figure 13). Contributions of corticocortical polysynaptic connections were also suggested by other groups (Hishida et al., 2014; Lim et al., 2012; Mohajerani et al., 2013). The long-lasting temporal window could be retained by phase-locking, which may increase the precision of multimodal integrated information and make selective attention more effective.

I observed phase-locking mainly in the excitatory network (Figures 10D and 10E, left). In contrast, the S+A+V stimulus induced a significantly larger power of slow oscillation at the late period compared with the S single stimulus in the inhibitory network, whereas there was no significant difference in the excitatory network (Figures 10D and 10E, right). These results suggest

that excitatory and inhibitory circuits have distinct roles (Gogolla et al., 2014; Iurilli et al., 2012; Olcese et al., 2013; Song et al., 2017). Given that slow waves reach from distant areas and mutually intensify at the association areas, I observed phase-locking in the excitatory network because long-range inputs are predominant in the network. Recently, it has been reported that impairment of slow-oscillation synchronization between the cerebral hemispheres in an Alzheimer's disease model mouse was recovered by a GABA agonist (Busche et al., 2015). Moreover, entrainment of cortical oscillatory activity is controlled by thalamocortical inputs via inhibitory neurons (Lemieux et al., 2014; O'Connell et al., 2011). Alteration of PLF patterns with isoflurane anesthesia, which mainly works as GABAa agonist (Figure 14E), and enhancement of PLF degrees with local neural inactivation by muscimol (Figure 13) can support the contribution of inhibitory neural population for the phase-locking induction. These results suggest that inhibitory neurons modulate synchronization of cortical slow oscillation.

It is not conclusive whether the phase locking actually important in multisensory integration or not, because performance of sensory association were not evaluated. To assess it, I should combine a multisensory association task with the wide-field calcium imaging. tLSL-YC2.60 mice express FRET based calcium sensor (YC2.60), which has large noise immunity than single fluorescence protein-based sensors such as GCaMPs (Grienberger and Konnerth, 2012). The advantage is suitable for combining behavior experiments because noises from body movement of mice during behavior are one of major problems for many types of fluorescence recordings, and FRET sensor can cancel them. In this study, I analyzed population calcium signals, including calcium fluctuation changes of each neurons and synchronization degree among the neurons, but still unclear how each single neuron behaves during the phase locking. Two-photon imaging or multi-unit recording can be used for analyzing activities of single neurons under the multisensory stimulus and answer the question. As a technical point, I think the application range of the cell-type specific wide-field calcium imaging method is very wide. In addition to advantages I showed in this

study, it can perform over months with the same subjects because of low invasiveness. This can make it possible to observe chronic process of learning, development, recovery from injury, mental disease and so on over whole cortex range.

References

Akemann, W., Mutoh, H., Perron, A., Park, Y.K., Iwamoto, Y., Knöpfel, T., 2012. Imaging neural circuit dynamics with a voltage-sensitive fluorescent protein. J. Neurophysiol. 108, 2323–2337.

Akemann, W., Mutoh, H., Perron, A., Rossier, J., Knöpfel, T., 2010. Imaging brain electric signals with genetically targeted voltage-sensitive fluorescent proteins. Nat. Methods 7, 643–649.

Akerboom, J., Chen, T.-W., Wardill, T.J., Tian, L., Marvin, J.S., Mutlu, S., Calderon, N.C., Esposti, F., Borghuis, B.G., Sun, X.R., Gordus, A., Orger, M.B., Portugues, R., Engert, F., Macklin, J.J., Filosa, A., Aggarwal, A., Kerr, R.A., Takagi, R., Kracun, S., Shigetomi, E., Khakh, B.S., Baier, H., Lagnado, L., Wang, S.S.-H., Bargmann, C.I., Kimmel, B.E., Jayaraman, V., Svoboda, K., Kim, D.S., Schreiter, E.R., Looger, L.L., 2012. Optimization of a GCaMP Calcium Indicator for Neural Activity Imaging. J. Neurosci. 32, 13819–13840.

Allen, W.E., Kauvar, I.V., Chen, M.Z., Deverman, B.E., Luo, L., Deisseroth, K., (2017). Global Representations of goal-directed behavior in distinct cell types of mouse neocortex. Neuron 94, 891-907

Andermann, M.L., Kerlin, A.M., Roumis, D.K., Glickfeld, L.L., Reid, R.C., 2011. Functional specialization of mouse higher visual cortical areas. Neuron 72, 1025–1039.

Aronoff, R., Matyas, F., Mateo, C., Ciron, C., Schneider, B., Petersen, C.C.H., 2010. Long-range connectivity of mouse primary somatosensory barrel cortex. Eur. J. Neurosci. 31, 2221–2233.

Aru, J., Aru, J., Priesemann, V., Wibral, M., Lana, L., Pipa, G., Singer, W., Vicente, R., 2015. Untangling cross-frequency coupling in neuroscience. Curr. Opin. Neurobiol. 31, 51–61.

Bellay, T., Klaus, A., Seshadri, S., Plenz, D., 2015. Irregular spiking of pyramidal neurons organizes as scale-invariant neuronal avalanches in the awake state. eLife 4, e07224.

Berridge, M.J., Lipp, P., Bootman, M.D., 2000. The versatility and universality of calcium signalling. Nat. Rev. Mol. Cell Biol. 1, 11–21

Binder, L.I., Frankfurter, A., Rebhun, L.I., 1985. The distribution of tau in the mammalian central

nervous system. J. Cell Biol. 101, 1371–1378.

Brett-Green, B., Fifková, E., Larue, D.T., Winer, J.A., Barth, D.S., 2003. A multisensory zone in rat parietotemporal cortex: intra- and extracellular physiology and thalamocortical connections. J. Comp. Neurol. 460, 223–237.

Bruce, C., Desimone, R., Gross, C.G., 1981. Visual properties of neurons in a polysensory area in superior temporal sulcus of the macaque. J. Neurophysiol. 46, 369–384.

Busche, M.A., Kekuš, M., Adelsberger, H., Noda, T., Förstl, H., Nelken, I., Konnerth, A., 2015. Rescue of long-range circuit dysfunction in Alzheimer's disease models. Nat. Neurosci. 18, 1623–1630.

Carandini, M., Shimaoka, D., Rossi, L.F., Sato, T.K., Benucci, A., Knöpfel, T., 2015. Imaging the awake visual cortex with a genetically encoded voltage indicator. J. Neurosci. 35, 53–63.

Chauvette, S., Crochet, S., Volgushev, M., Timofeev, I., 2011. Properties of slow oscillation during slow-wave sleep and anesthesia in cats. J. Neurosci. 31, 14998–15008.

Chen, I.-W., Helmchen, F., Lütcke, H., 2015. Specific early and late oddball-evoked responses in excitatory and inhibitory neurons of mouse auditory cortex. J. Neurosci. 35, 12560–12573.

Chen, T.-W., Wardill, T.J., Sun, Y., Pulver, S.R., Renninger, S.L., Baohan, A., Schreiter, E.R., Kerr, R. a, Orger, M.B., Jayaraman, V., Looger, L.L., Svoboda, K., Kim, D.S., 2013. Ultrasensitive fluorescent proteins for imaging neuronal activity. Nature 499, 295–300.

Choi, J.-H., Yu, N.-K., Baek, G.-C., Bakes, J., Seo, D., Nam, H.J., Baek, S.H., Lim, C.-S., Lee, Y.-S., Kaang, B.-K., 2014. Optimization of AAV expression cassettes to improve packaging capacity and transgene expression in neurons. Mol. Brain 7, 17.

Duhamel, J.-R.R., Colby, C.L., Goldberg, M.E., 1998. Ventral intraparietal area of the macaque: congruent visual and somatic response properties. J. Neurophysiol. 79, 126–136.

Farley, B.J., Noreña, A.J., 2013. Spatiotemporal coordination of slow-wave ongoing activity across auditory cortical areas. J. Neurosci. 33, 3299–3310.

Fell, J., Axmacher, N., 2011. The role of phase synchronization in memory processes. Nat. Rev. Neurosci. 12, 105–118.

Ferezou, I., Haiss, F., Gentet, L.J., Aronoff, R., Weber, B., Petersen, C.C.H., 2007. Spatiotemporal dynamics of cortical sensorimotor integration in behaving mice. Neuron 56, 907–923.

Fucke, T., Suchanek, D., Nawrot, M.P., Seamari, Y., Heck, D.H., Aertsen, A., Boucsein, C., 2011. Stereotypical spatiotemporal activity patterns during slow-wave activity in the neocortex. J. Neurophysiol. 106, 3035–3044.

Fujisawa, S., Buzsáki, G., 2011. A 4 Hz oscillation adaptively synchronizes prefrontal, VTA, and hippocampal activities. Neuron 72, 153–165.

Funayama, K., Minamisawa, G., Matsumoto, N., Ban, H., Chan, A.W., Matsuki, N., Murphy, T.H., Ikegaya, Y., 2015. Neocortical rebound depolarization enhances visual perception. PLoS Biol. 13, e1002231.

Ghazanfar, A.A., Schroeder, C.E., 2006. Is neocortex essentially multisensory? Trends Cogn. Sci. 10, 278–85.

Gogolla, N., Takesian, A.E., Feng, G., Fagiolini, M., Hensch, T.K., 2014. Sensory integration in mouse insular cortex reflects GABA circuit maturation. Neuron 83, 894–905.

Grienberger, C., Adelsberger, H., Stroh, A., Milos, R.-I., Garaschuk, O., Schierloh, A., Nelken, I., Konnerth, A., 2012. Sound-evoked network calcium transients in mouse auditory cortex in vivo. J. Physiol. 590, 899–918.

Grienberger, C., Konnerth, A., 2012. Imaging calcium in neurons. Neuron 73, 862–885.

Haider, B., Duque, A., Hasenstaub, A.R., McCormick, D.A., 2006. Neocortical network activity in vivo is generated through a dynamic balance of excitation and inhibition. J. Neurosci. 26, 4535–4545.

Haider, B., Häusser, M., Carandini, M., 2013. Inhibition dominates sensory responses in the awake cortex. Nature 493, 97–100.

Harris, J.A., Hirokawa, K.E., Sorensen, S.A., Gu, H., Mills, M., Ng, L.L., Bohn, P., Mortrud, M., Ouellette, B., Kidney, J., Smith, K.A., Dang, C., Sunkin, S., Bernard, A., Oh, S.W., Madisen, L., Zeng, H., 2014. Anatomical characterization of Cre driver mice for neural circuit mapping and manipulation. Front. Neural Circuits 8, 76.

Harvey, C.D., Coen, P., Tank, D.W., 2012. Choice-specific sequences in parietal cortex during a virtual-navigation decision task. Nature 484, 62–68.

Hintiryan, H., Gou, L., Song, M.Y., Bay, M., Bienkowski, M.S., Foster, N.N., Yamashita, S., Bowman, I., Toga, A.W., Dong, H.-W., 2014. Neural networks of the mouse neocortex. Cell 156, 1096–1111.

Hishida, R., Kudoh, M., Shibuki, K., 2014. Multimodal cortical sensory pathways revealed by sequential transcranial electrical stimulation in mice. Neurosci. Res. 87, 49–55.

Horikawa, K., Yamada, Y., Matsuda, T., Kobayashi, K., Hashimoto, M., Matsu-ura, T., Miyawaki, A., Michikawa, T., Mikoshiba, K., Nagai, T., 2010. Spontaneous network activity visualized by ultrasensitive Ca^{2+} indicators, yellow Cameleon-Nano. Nat. Methods 7, 729–732.

Husson, T.R., Mallik, A.K., Zhang, J.X., Issa, N.P., 2007. Functional imaging of primary visual cortex using flavoprotein autofluorescence. J. Neurosci. 27, 8665–8675.

Iurilli, G., Ghezzi, D., Olcese, U., Lassi, G., Nazzaro, C., Tonini, R., Tucci, V., Benfenati, F., Medini, P., 2012. Sound-driven synaptic inhibition in primary visual cortex. Neuron 73, 814–828.

Iwasato, T., Datwani A., Wolf A.M., Nishiyama H., Taguchi Y., Tonegawa S., Knöpfel T., Erzurumlu R.S., Itohara S., 2000. Cortex-restricted disruption of NMDAR1 impairs neuronal patterns in the barrel cortex. Nature 406, 726–731.

Jansen, M., 2001. Noise Reduction by Wavelet Thresholding, Lecture Notes in Statistics. Springer, New York, NY.

Jain, A.K., and Dubes, R.C., 1988. Algorithms for clustering data, Prentice Hall.

Kalatsky, V.A., Polley, D.B., Merzenich, M.M., Schreiner, C.E., Stryker, M.P., 2005. Fine functional organization of auditory cortex revealed by Fourier optical imaging. Proc. Natl. Acad. Sci. U. S. A. 102, 13325–13330.

Kayser, C., Petkov, C.I., Logothetis, N.K., 2008. Visual modulation of neurons in auditory cortex. Cereb. Cortex 18, 1560–1574.

Kenet, T., Bibitchkov, D., Tsodyks, M., Grinvald, A., Arieli, A., 2003. Spontaneously emerging cortical

representations of visual attributes. Nature 425, 954–956.

Kerr, J.N.D., Greenberg, D., Helmchen, F., 2005. Imaging input and output of neocortical networks in vivo. Proc. Natl. Acad. Sci. U. S. A. 102, 14063–14068.

Kirkcaldie, M.T.K., 2012. Neocortex, in: Watson, C., Paxinos, G., Puelles, L. (Eds.), The Mouse Nervous System. Academic Press, San Diego, CA, pp. 52–111.

Knöpfel, T., 2012. Genetically encoded optical indicators for the analysis of neuronal circuits. Nat. Rev. Neurosci. 13, 687–700.

Koresawa, Y., Miyagawa, S., Ikawa, M., Matsunami, K., Yamada, M., Shirakura, R., Okabe, M., 2000. Synthesis of a new Cre recombinase gene based on optimal codon usage for mammalian systems. J. Biochem. 127, 367–372.

Kuroki, S., Yoshida, T., Tsutsui, H., Iwama, M., Ando, R., Michikawa, T., Miyawaki, A., Ohshima, T., Itohara, S., 2018. Excitatory neuronal hubs configure multisensory integration of slow waves in association cortex. Cell Rep., in press

Lakatos, P., Chen, C.-M., O'Connell, M.N., Mills, A., Schroeder, C.E., 2007. Neuronal oscillations and multisensory interaction in primary auditory cortex. Neuron 53, 279–292.

Lakatos, P., Musacchia, G., O'Connel, M.N., Falchier, A.Y., Javitt, D.C., Schroeder, C.E., 2013. The spectrotemporal filter mechanism of auditory selective attention. Neuron 77, 750–761.

Lee, C.C., Sherman, S.M., 2010. Topography and physiology of ascending streams in the auditory tectothalamic pathway. Proc. Natl. Acad. Sci. U. S. A. 107, 372–377.

Lemieux, M., Chauvette, S., Timofeev, I., 2015. Neocortical inhibitory activities and long-range afferents contribute to the synchronous onset of silent states of the neocortical slow oscillation. J. Neurophysiol. 2, 768-779.

Lim, D.H., Mohajerani, M.H., LeDue, J., Boyd, J., Chen, S., Murphy, T.H., 2012. In vivo large-scale cortical mapping using channelrhodopsin-2 stimulation in transgenic mice reveals asymmetric and reciprocal relationships between cortical areas. Front. Neural Circuits 6, 11.

Lin, M.Z., Schnitzer, M.J., 2016. Genetically encoded indicators of neuronal activity. Nat. Neurosci. 19,

1142–1153.

Lippert, M.T., Takagaki, K., Kayser, C., Ohl, F.W., 2013. Asymmetric multisensory interactions of visual and somatosensory responses in a region of the rat parietal cortex. PLoS One 8, e63631.

Luczak, A., Barthó, P., Marguet, S.L., Buzsáki, G., Harris, K.D., 2007. Sequential structure of neocortical spontaneous activity in vivo. Proc. Natl. Acad. Sci. U. S. A. 104, 347–352.

Luo, L., Callaway, E.M., Svoboda, K., 2008. Genetic dissection of neural circuits. Neuron 57, 634–60.

Lütcke, H., Murayama, M., Hahn, T., Margolis, D.J., Astori, S., Zum Alten Borgloh, S.M., Göbel, W., Yang, Y., Tang, W., Kügler, S., Sprengel, R., Nagai, T., Miyawaki, A., Larkum, M.E., Helmchen, F., Hasan, M.T., 2010. Optical recording of neuronal activity with a genetically-encoded calcium indicator in anesthetized and freely moving mice. Front. Neural Circuits 4, 9.

Madisen, L., Garner, A.R., Shimaoka, D., Chuong, A.S., Klapoetke, N.C., Li, L., van der Bourg, A., Niino, Y., Egolf, L., Monetti, C., Gu, H., Mills, M., Cheng, A., Tasic, B., Nguyen, T.N., Sunkin, S.M., Benucci, A., Nagy, A., Miyawaki, A., Helmchen, F., Empson, R.M., Knöpfel, T., Boyden, E.S., Reid, R.C., Carandini, M., Zeng, H., 2015. Transgenic mice for intersectional targeting of neural sensors and effectors with high specificity and performance. Neuron 85, 942–958.

Makino, H., Komiyama, T., 2015. Learning enhances the relative impact of top-down processing in the visual cortex. Nat. Neurosci. 18, 1116–1122.

Makino, H., Ren, C., Liu, H., Kim, A.N., Kondapaneni, N., Liu, X., Kuzum, D., Komiyama, T. 2017. Transformation of Cortex-wide Emergent Properties during Motor Learning. Neuron 94, 880-890.

Manita, S., Suzuki, T., Homma, C., Matsumoto, T., Odagawa, M., Yamada, K., Ota, K., Matsubara, C., Inutsuka, A., Sato, M., Ohkura, M., Yamanaka, A., Yanagawa, Y., Nakai, J., Hayashi, Y., Larkum, M.E., Murayama, M., 2015. A top-down cortical circuit for accurate sensory perception. Neuron 86, 1304–1316.

Manly, T., Hawkins, K., Evans, J., Woldt, K., Robertson, I.H., 2002. Rehabilitation of executive function: Facilitation of effective goal management on complex tasks using periodic auditory alerts. Neuropsychologia 40, 271–281.

Markram, H., Toledo-Rodriguez, M., Wang, Y., Gupta, A., Silberberg, G., Wu, C., 2004. Interneurons of the neocortical inhibitory system. Nat. Rev. Neurosci. 5, 793–807.

McCormick, D.A., McGinley, M.J., Salkoff, D.B., 2015. Brain state dependent activity in the cortex and thalamus. Curr. Opin. Neurobiol. 31, 133–140.

Meredith, M.A., Stein, B.E., 1983. Interactions among converging sensory inputs in the superior colliculus. Science 221, 389–391.

Minderer, M., Liu, W., Sumanovski, L.T., Kügler, S., Helmchen, F., Margolis, D.J., 2012. Chronic imaging of cortical sensory map dynamics using a genetically encoded calcium indicator. J. Physiol. 590, 99–107.

Mohajerani, M.H., Chan, A.W., Mohsenvand, M., Ledue, J., Liu, R., McVea, D. a, Boyd, J.D., Wang, Y.T., Reimers, M., Murphy, T.H., 2013. Spontaneous cortical activity alternates between motifs defined by regional axonal projections. Nat. Neurosci. 16, 1426–1435.

Mohajerani, M.H., McVea, D., Fingas, M., Murphy, T.H., 2010. Mirrored bilateral slow-wave cortical activity within local circuits revealed by fast bihemispheric voltage-sensitive dye imaging in anesthetized and awake mice. J. Neurosci. 30, 3745–3751.

Monai, H., Ohkura, M., Tanaka, M., Oe, Y., Konno, A., Hirai, H., Mikoshiba, K., Itohara, S., Nakai, J., Iwai, Y., Hirase, H., 2016. Calcium imaging reveals glial involvement in transcranial direct current stimulation-induced plasticity in mouse brain. Nat. Commun. 7, 11100.

Murakami, T., Yoshida, T., Matsui, T., Ohki, K., 2015. Wide-field Ca^{2+} imaging reveals visually evoked activity in the retrosplenial area. Front. Mol. Neurosci. 08, 20.

Nagai, T., Yamada, S., Tominaga, T., Ichikawa, M., Miyawaki, A., 2004. Expanded dynamic range of fluorescent indicators for Ca^{2+} by circularly permuted yellow fluorescent proteins. Proc. Natl. Acad. Sci. U. S. A. 101, 10554–10559.

Neske, G.T., Patrick, S.L., Connors, B.W., 2015. Contributions of diverse excitatory and inhibitory neurons to recurrent network activity in cerebral cortex. J. Neurosci. 35, 1089–1105.

O'Connell, M.N., Falchier, A., McGinnis, T., Schroeder, C.E., Lakatos, P., 2011. Dual Mechanism of

Neuronal Ensemble Inhibition in Primary Auditory Cortex. Neuron 69, 805–817.

Ogiwara, I., Iwasato, T., Miyamoto, H., Iwata, R., Yamagata, T., Mazaki, E., Yanagawa, Y., Tamamaki, N., Hensch, T.K., Itohara, S., Yamakawa, K., 2013. Nav1.1 haploinsufficiency in excitatory neurons ameliorates seizure-associated sudden death in a mouse model of Dravet syndrome. Hum. Mol. Genet. 22, 4784–4804.

Okun, M., Lampl, I., 2008. Instantaneous correlation of excitation and inhibition during ongoing and sensory-evoked activities. Nat. Neurosci. 11, 535–537.

Olcese, U., Iurilli, G., Medini, P., 2013. Cellular and synaptic architecture of multisensory integration in the mouse neocortex. Neuron 79, 579–593.

Palmiter, R.D., Sandgren, E.P., Avarbock, M.R., Allen, D.D., Brinster, R.L., 1991. Heterologous introns can enhance expression of transgenes in mice. Proc. Natl. Acad. Sci. U. S. A. 88, 478–82.

Petreanu, L., Huber, D., Sobczyk, A., Svoboda, K., 2007. Channelrhodopsin-2-assisted circuit mapping of long-range callosal projections. Nat. Neurosci. 10, 663–668.

Reig, R., Silberberg, G., 2014. Multisensory integration in the mouse striatum. Neuron 83, 1200–1212.

Robinson, S., Keene, C.S., Iaccarino, H.F., Duan, D., Bucci, D.J., 2011. Involvement of retrosplenial cortex in forming associations between multiple sensory stimuli. Behav. Neurosci. 125, 578–587.

Rohr, U.-P., Wulf, M.-A., Stahn, S., Steidl, U., Haas, R., Kronenwett, R., 2002. Fast and reliable titration of recombinant adeno-associated virus type-2 using quantitative real-time PCR. J. Virol. Methods 106, 81–88.

Saitoh, K., Inagaki, S., Nishimura, M., Kawaguchi, H., Song, W.J., 2010. Spontaneous activity resembling tone-evoked activity in the primary auditory cortex of guinea pigs. Neurosci. Res. 68, 107–113.

Samulski, R.J., Chang, L.S., Shenk, T., 1989. Helper-free stocks of recombinant adeno-associated viruses: normal integration does not require viral gene expression. J. Virol. 63, 3822–3828.

Schroeder, C.E., Foxe, J., 2005. Multisensory contributions to low-level, “unisensory” processing. Curr. Opin. Neurobiol. 15, 454–458.

Schroeder, C.E., Lakatos, P., 2009. Low-frequency neuronal oscillations as instruments of sensory selection. Trends Neurosci. 32, 9–18.

Schuett, S., Bonhoeffer, T., Hübener, M., 2002. Mapping retinotopic structure in mouse visual cortex with optical imaging. J. Neurosci. 22, 6549–6559.

Sheroziya, M., Timofeev, I., 2014. Global intracellular slow-wave dynamics of the thalamocortical system. J. Neurosci. 34, 8875–8893.

Shibuki, K., Hishida, R., Murakami, H., Kudoh, M., Kawaguchi, T., Watanabe, M., Watanabe, S., Kouuchi, T., Tanaka, R., 2003. Dynamic imaging of somatosensory cortical activity in the rat visualized by flavoprotein autofluorescence. J Physiol. 549, 919–927

Sieben, K., Röder, B., Hanganu-Opatz, I.L., 2013. Oscillatory entrainment of primary somatosensory cortex encodes visual control of tactile processing. J. Neurosci. 33, 5736–5749.

Song, Y., Kim, J.-H., Jeong, H.-W., Choi, I., Jeong, D., Kim, K., Lee, S., 2017. A neural circuit for auditory dominance over visual perception. Neuron *93*, 940–954.

Stein, B.E., Stanford, T.R., 2008. Multisensory integration: current issues from the perspective of the single neuron. Nat. Rev. Neurosci. 9, 255–266.

Steriade, M., Nuñez, A., Amzica, F., 1993. A novel slow (< 1 Hz) oscillation of neocortical neurons in vivo: depolarizing and hyperpolarizing components. J. Neurosci. 13, 3252–3265.

Stroh, A., Adelsberger, H., Groh, A., Rühlmann, C., Fischer, S., Schierloh, A., Deisseroth, K., Konnerth, A., 2013. Making waves: initiation and propagation of corticothalamic Ca^{2+} waves in vivo. Neuron 77, 1136–1150.

Sugihara, T., Diltz, M.D., Averbeck, B.B., Romanski, L.M., 2006. Integration of auditory and visual communication information in the primate ventrolateral prefrontal cortex. J. Neurosci. 26, 11138–11147.

Takahashi, K., Hishida, R., Kubota, Y., Kudoh, M., Takahashi, S., Shibuki, K., 2006. Transcranial fluorescence imaging of auditory cortical plasticity regulated by acoustic environments in mice. Eur. J. Neurosci. 23, 1365–1376.

Takeshita, S., Sato, M., Toba, M., Masahashi, W., Hashimoto-Gotoh, T., 1987. High-copy-number and low-copy-number plasmid vectors for lacZ alpha-complementation and chloramphenicol- or kanamycin-resistance selection. Gene 61, 63–74.

Takita, K., Aoki, T., Sasaki, Y., Higuchi, T., and Kobayashi, K., 2003. High-Accuracy Subpixel Image Registration Based on Phase-Only Correlation. IEICE Trans. Fundam. Electron. Commun. Comput. Sci. 86, 1925–1934.

Tamamaki, N., Tomioka, R., 2010. Long-range GABAergic connections distributed throughout the neocortex and their possible function. Front. Neurosci. 4, 202.

Theyel, B.B., Llano, D. a, Sherman, S.M., 2010. The corticothalamocortical circuit drives higher-order cortex in the mouse. Nat. Neurosci. 13, 84–88.

Tsutsui, H., Jinno, Y., Tomita, A., Niino, Y., Yamada, Y., Mikoshiba, K., Miyawaki, A., Okamura, Y., 2013. Improved detection of electrical activity with a voltage probe based on a voltage-sensing phosphatase. J. Physiol. 591, 4427–4437.

van Atteveldt, N., Murray, M.M., Thut, G., Schroeder, C.E., 2014. Multisensory integration: flexible use of general operations. Neuron 81, 1240–1253.

Vanni, M.P., Murphy, T.H., 2014. Mesoscale transcranial spontaneous activity mapping in GCaMP3 transgenic mice reveals extensive reciprocal connections between areas of somatomotor cortex. J. Neurosci. 34, 15931–15946.

Varela, F., Lachaux, J.P., Rodriguez, E., Martinerie, J., 2001. The brainweb: phase synchronization and large-scale integration. Nat. Rev. Neurosci. 2, 229–239.

Vyazovskiy, V. V, Faraguna, U., Cirelli, C., Tononi, G., 2009. Triggering slow waves during NREM sleep in the rat by intracortical electrical stimulation: effects of sleep/wake history and background activity. J. Neurophysiol. 101, 1921–1931.

Wallace, M.T., Ramachandran, R., Stein, B.E., 2004. A revised view of sensory cortical parcellation. Proc. Natl. Acad. Sci. U. S. A. 101, 2167–2172.

Wang, Q., Sporns, O., Burkhalter, A., 2012. Network analysis of corticocortical connections reveals

ventral and dorsal processing streams in mouse visual cortex. J. Neurosci. 32, 4386–4399.

Weiss, S., Rappelsberger, P., 2000. Long-range EEG synchronization during word encoding correlates with successful memory performance. Cogn. Brain Res. 9, 299–312.

White, B.R., Bauer, A.Q., Snyder, A.Z., Schlaggar, B.L., Lee, J.M., Culver, J.P., 2011. Imaging of functional connectivity in the mouse brain. PLoS One 6, e16322.

Wilber, A. a, Clark, B.J., Demecha, A.J., Mesina, L., Vos, J.M., McNaughton, B.L., 2015. Cortical connectivity maps reveal anatomically distinct areas in the parietal cortex of the rat. Front. Neural Circuits 8, 146.

Xu, W., Huang, X., Takagaki, K., Wu, J.Y., 2007. Compression and reflection of visually evoked cortical waves. Neuron 55, 119–129.

Yoshida, T., Sakagami, M., Katura, T., Yamazaki, K., Tanaka, S., Iwamoto, M., Tanaka, N., 2008. Anisotropic spatial coherence of ongoing and spontaneous activities in auditory cortex. Neurosci. Res. 61, 49–55.

Yoshida, T., Ozawa, K., and Tanaka, S., 2012. Sensitivity profile for orientation selectivity in the visual cortex of goggle-reared mice. PLoS One 7, e40630.

Yoshitake, K., Tsukano, H., Tohmi, M., Komagata, S., Hishida, R., Yagi, T., Shibuki, K., 2013. Visual Map Shifts based on Whisker-Guided Cues in the Young Mouse Visual Cortex. Cell Rep. 5, 1365–1374.

Zariwala, H.A., Borghuis, B.G., Hoogland, T.M., Madisen, L., Tian, L., De Zeeuw, C.I., Zeng, H., Looger, L.L., Svoboda, K., Chen, T.-W., 2012. A Cre-dependent GCaMP3 reporter mouse for neuronal imaging in vivo. J. Neurosci. 32, 3131–41.

Zhang, F., Gradinaru, V., Adamantidis, A.R., Durand, R., Airan, R.D., de Lecea, L., Deisseroth, K., 2010. Optogenetic interrogation of neural circuits: technology for probing mammalian brain structures. Nat. Protoc. 5, 439–456.

Acknowledgements

I would like to express my devout gratitude to my supervisors, Prof. Toshio Ohshima, Professor of Laboratory for Molecular Brain Science, Graduate School of Advance Science and Engineering, Department of Life Science & Medical Science, Waseda University, and Prof. Shigeyoshi Itohara, Senior Team Leader of Laboratory for Behavior Genetics, RIKEN Brain Science Institute, for their helpful advices and supports, and providing me the wonderful opportunity to study in such a great environment.

I greatly appreciate Dr. Takamasa Yoshida, Dr. Kunio Yaguchi and the other previous and current members of Laboratory for Behavior Genetics kindly teaching me various experimental and analytical methods, discussing about many topics for a so long time and guiding this project. I am grateful to Prof. Atsushi Miyawaki, Prof. Hidekazu Tsutsui, Dr. Takayuki Michikawa and the other members of Laboratory for Cell Function Dynamics, RIKEN Brain Science Institute, for generous collaboration and allowing me to use their laboratory experimental space and equipment.

Finally, I would like to express my grateful thanks to my family. They gave me persistent support and encouragement through my entire life.

This work was supported in part by Grant-in-Aid for Japan Society for the Promotion of Sciences (JSPS) Fellows (12J00301), Grant-in-Aid for Young Scientists (B) from JSPS (25871135), the program for Brain Mapping by Integrated Neurotechnologies for Disease Studies (Brain/MINDS) from the Japan Agency for Medical Research and Development (AMED), The Ministry of Education, Culture, Sports, Science and Technology (MEXT)-Supported Program for the Strategic Research Foundation at Private Universities, 2012–2016, and Funding Program for World-Leading Innovative R&D on Science and Technology (FIRST Program) initiated by the Council for Science and Technology Policy (CSTP).

Achievements

Articles

Satoshi Kuroki, Takamasa Yoshida, Hidekazu Tsutsui, Mizuho Iwama, Reiko Ando, Takayuki Michikawa, Atsushi Miyawaki, Toshio Ohshima and Shigeyoshi Itohara, “Excitatory neuronal hubs configure multisensory integration of slow waves in association cortex”, Cell Reports, in press

Kunio Yaguchi, Sachiko Nishimura-Akiyoshi, **Satoshi Kuroki**, Takashi Onodera and Shigeyoshi Itohara, "Identification of transcriptional regulatory elements for Ntng1 and Ntng2 genes in mice", Molecular Brain, 7:19, 2014

Presentations

Satoshi Kuroki, Takamasa Yoshida, Hidekazu Tsutsui, Takayuki Michikawa, Mizuho Iwama, Atsushi Miyawaki, Shigeyoshi Itohara, " Cell-type-specific calcium imaging of cortical slow oscillation reveals phase-locking induced by multisensory inputs", FENS Forum 2016, Federation of European Neurosciences Societies, FENS-3413, Copenhagen, Denmark, July 2016, Poster

Satoshi Kuroki, Hidekazu Tsutsui, Takayuki Michikawa, Mizuho Iwama, Atsushi Miyawaki, Shigeyoshi Itohara, "Cell-type selective transcranial wide-field calcium imaging combined with Yellow Cameleon 2.60 transgenic mice and macro-zoom microscopy", Neuroscience2013, 488.20/MMM37, Sosciety for Neuroscience, San Diego, the United States, November 2013, Poster

Satoshi Kuroki, Hidekazu Tsutsui, Takayuki Michikawa, Mizuho Iwama, Atsushi Miyawaki, Shigeyoshi Itohara, "Cell-type selective transcranial wide-field calcium imaging combined with Yellow Cameleon 2.60 transgenic mice and macro-zoom microscopy", Optogenetics2013, Tokyo, September 2013, Poster

Satoshi Kuroki, Hidekazu Tsutsui, Takayuki Michikawa, Mizuho Iwama, Atsushi Miyawaki, Shigeyoshi Itohara, "Cell-type selective wide-field calcium imaging combined with Yellow Cameleon 2.60 Transgenic mice and macromicroscopy", MCCS-Asia, Kyoto, June 2013, Poster

Satoshi Kuroki, Takayuki Michikawa, Satoshi Manita, Hidekazu Tsutsui, Satoshi Shimozono,

Masanori Murayama, Atsushi Miyawaki, Shigeyoshi Itohara, "Cell-type selective wide-field calcium imaging, by combining Yellow Cameleon 2.60 Tg mice and macromicroscopy", Circuit construction in the mammalian cerebral cortex: Genetic and imaging approaches, Shizuoka, December 2012, Poster

Satoshi Kuroki, Takayuki Michikawa, Hidekazu Tsutsui, Satoshi Manita, Satoshi Shimozono, Masanori Murayama, Atsushi Miyawaki, Shigeyoshi Itohara, "Cell-type selective wide-field calcium imaging, combined Yellow Cameleon 2.60 Tg mice and macromicroscopy" Eleventh Annual MCCS meeting, New Orleans, the United States, October 2012, Poster

Satoshi Kuroki, Takayuki Michikawa, Satoshi Manita, Hidekazu Tsutsui, Satoshi Shimozono, Masanori Murayama, Atsushi Miyawaki, Shigeyoshi Itohara, "Establishment of transgenic mice expressing calcium sensor Yellow Cameleon 2.60 and applications to analysis of the thalamocortical pathway", The 35th Annual Meeting of Japan Neuroscience Society, P1-k14, Aichi, September 2012, Poster

Satoshi Kuroki, Takayuki Michikawa, Satoshi Manita, Hidekazu Tsutsui, Satoshi Shimozono, Masanori Murayama, Atsushi Miyawaki, Shigeyoshi Itohara, "Establishment of transgenic mice expressing calcium sensor Yellow Cameleon 2.60 and applications to analysis of the thalamocortical pathway", BMAP 2012, Tokyo, August 2012, Poster